

Improving the constraint on the Mw 7.1 2016 off-Fukushima shallow normal-faulting earthquake with the high azimuthal coverage tsunami data from the S-net wide and dense network: Implication for the stress regime in the Tohoku overriding plate

Tatsuya Kubota¹, Hisahiko Kubo¹, Keisuke Yoshida², Naotaka Yamamoto Chikasada¹, Wataru Suzuki¹, Takeshi Nakamura³, and Hiroaki Tsushima⁴

¹National Research Institute for Earth Science and Disaster Resilience

²Tohoku University

³Central Research Institute of Electric Power Industry

⁴Meteorological Research Institute

November 26, 2022

Abstract

Tsunamis with maximum amplitudes of up to 40 cm, related to the M_w 7.1 normal-faulting earthquake off Fukushima, Japan, on November 21, 2016 (UTC), were clearly recorded by a new offshore wide and dense ocean bottom pressure gauge network, S-net, with high azimuthal coverage located closer to the focal area. We processed the S-net data and found that some stations included the tsunami-irrelevant drift and step signals. We then analyzed the S-net data to infer the tsunami source distribution. A subsidence region with a narrow spatial extent (~ 40 km) and a large peak (~ 200 cm) was obtained. The other near-coastal waveforms not used for the inversion analysis were also reproduced very well. Our fault model suggests that the stress drop of this earthquake is ~ 10 MPa, whereas the shear stress increase along the fault caused by the 2011 Tohoku earthquake was only ~ 2 MPa. Past studies have suggested that horizontal compressional stress around this region switched to horizontal extensional stress after the Tohoku earthquake due to the stress change. The present result, however, suggests that the horizontal extensional stress was locally predominant at the shallowest surface around this region even before the 2011 Tohoku earthquake. The present study demonstrates that the S-net high-azimuthal-coverage pressure data provides a significant constraint on the fault modeling, which enables us to discuss the stress regime within the overriding plate around the offshore region. Our analysis provides an implication for the crustal stress state, which is important for understanding the generation mechanisms of the intraplate earthquake.

Improving the constraint on the M_w 7.1 2016 off-Fukushima shallow normal-faulting earthquake with the high azimuthal coverage tsunami data from the S-net wide and dense network: Implication for the stress regime in the Tohoku overriding plate

Tatsuya Kubota¹, Hisahiko Kubo¹, Keisuke Yoshida², Naotaka Y. Chikasada¹, Wataru Suzuki¹, Takeshi Nakamura³, and Hiroaki Tsushima⁴

¹ National Research Institute for Earth Science and Disaster Resilience, Tsukuba, Japan.

² Graduate School of Science, Tohoku University, Sendai, Japan.

³ Central Research Institute of Electric Power Industry, Abiko, Japan.

⁴ Meteorological Research Institute, Japan Meteorological Agency, Tsukuba, Japan

Corresponding author: Tatsuya Kubota (kubotatsu@bosai.go.jp)

Key Points:

- Tsunamis due to the 2016 off-Fukushima shallow normal-faulting earthquake were observed by the S-net wide and dense pressure gauge network
- Use of the near-field and the high-coverage array significantly improved the constraint of the fault modeling of the 2016 earthquake
- Our fault model suggested that the stress around the focal area should be in a normal-faulting regime even before the 2011 Tohoku earthquake

Abstract

Tsunamis with maximum amplitudes of up to 40 cm, related to the M_w 7.1 normal-faulting earthquake off Fukushima, Japan, on November 21, 2016 (UTC), were clearly recorded by a new offshore wide and dense ocean bottom pressure gauge network, S-net, with high azimuthal coverage located closer to the focal area. We processed the S-net data and found that some stations included the tsunami-irrelevant drift and step signals. We then analyzed the S-net data to infer the tsunami source distribution. A subsidence region with a narrow spatial extent (~ 40 km) and a large peak (~ 200 cm) was obtained. The other near-coastal waveforms not used for the inversion analysis were also reproduced very well. Our fault model suggests that the stress drop of this earthquake is ~ 10 MPa, whereas the shear stress increase along the fault caused by the 2011 Tohoku earthquake was only ~ 2 MPa. Past studies have suggested that horizontal compressional stress around this region switched to horizontal extensional stress after the Tohoku earthquake due to the stress change. The present result, however, suggests that the horizontal extensional stress was locally predominant at the shallowest surface around this region even before the 2011 Tohoku earthquake. The present study demonstrates that the S-net high-azimuthal-coverage pressure data provides a significant constraint on the fault modeling, which enables us to discuss the stress regime within the overriding plate around the offshore region. Our analysis provides an implication for the crustal stress state, which is important for understanding the generation mechanisms of the intraplate earthquake.

Plain Language Summary

On November 21, 2016 (UTC), a large earthquake occurred within the continental plate off Fukushima, Japan, and a new seafloor tsunami network, S-net, recorded its tsunamis with much higher azimuthal coverage and with shorter epicentral distance than any of the previous networks. We analyzed the S-net data to reveal the rupture process of this earthquake. Our result explained all of the S-net data and the other tsunami network data very well. According to past studies, the continental plate in northeastern Japan was under horizontal compression before the 2011 Tohoku earthquake due to the pushing force by the subducting oceanic plate. However, our rupture modeling result suggested that the plate around the earthquake rupture area was horizontally stretched even before the Tohoku earthquake, so that the off-Fukushima earthquake occurred. Our study demonstrated that the S-net, which has high spatial coverage, makes it

55 possible to reveal the rupture model of offshore earthquakes, which was difficult in the past
56 before S-net became available. The S-net will also enable us to discuss the impact of the Tohoku
57 earthquake on the crustal stress, which is necessary for understanding the earthquake generation
58 mechanics.

59

1 Introduction

In this decade, the coseismic rupture process of the 2011 Tohoku earthquake and its preseismic and postseismic processes have been investigated in detail (e.g., Hino, 2015; Kodaira et al., 2020; 2021; Lay, 2018; Uchida & Burgmann, 2021; Wang et al., 2018). In response to the Tohoku earthquake, a new wide offshore deep-ocean observation network, Seafloor Observation Network for Earthquakes and Tsunamis along the Japan Trench (S-net), has been constructed off eastern Japan (Aoi et al., 2020; Kanazawa et al., 2016; Mochizuki et al., 2017; Uehira et al., 2016, Figure 1a). Recent studies have started to utilize S-net ocean bottom seismometers to investigate the seismotectonics and geodynamics in the Tohoku subduction zone (Hua et al., 2020; Matsubara et al., 2019; Nishikawa et al., 2019; Sawazaki & Nakamura, 2020; Takagi et al., 2019, 2021; Tanaka et al., 2019; Uchida et al., 2020; Yu & Zhao, 2020). The S-net also incorporates ocean-bottom pressure gauges (OBPGs), which are expected to be utilized for tsunami forecasts (e.g., Aoi et al., 2019; Inoue et al., 2019; Mulia & Satake, 2021; Tanioka, 2020; Tsushima & Yamamoto, 2020; Wang et al., 2021; Yamamoto Aoi et al., 2016; Yamamoto, Hirata et al., 2016). The other potential contributions to the earth sciences of the S-net OBPG have also been demonstrated, such as understanding the wave propagation process in the ocean as well as the rupture process of subseafloor earthquakes (Kubota, Saito, & Suzuki, 2020; Kubota et al., 2021; Saito & Kubota, 2020; Saito et al., 2021). The wide and dense network data of S-net will significantly broaden our understanding of the Tohoku subduction zone after the Tohoku earthquake.

On November 21, 2016, a major shallow normal-faulting earthquake occurred within the overriding plate off Fukushima Prefecture (20:59 UTC, M_w 6.9, 12 km, Global CMT [GCMT], <https://www.globalcmt.org>, Figure 1, hereafter referred to as the off-Fukushima earthquake). Compared with the GCMT centroid, its epicenter, as determined by Japan Meteorological Agency (JMA), was located ~20 km east to northeast (white star in Figure 1). Numerous aftershocks accompanied this earthquake (Figures 1b and 1c). It has been reported that the tsunamis associated with the off-Fukushima earthquake were observed by onshore and offshore tsunami networks (e.g., Gusman et al., 2017; Kawaguchi et al., 2017; Suppasri et al., 2017). However, these stations were located only on the shore-side from the focal area, and the source-station distances are large (Figure 1a). In contrast, the S-net OBPGs recorded tsunamis with much higher azimuthal coverage and with a closer distance to the focal area (~30 km,

Figure 1a). Because of the much better station coverage of the S-net, the constraint on the initial sea height (tsunami source) estimation and the finite fault modeling of the off-Fukushima earthquake will be significantly increased, as compared with the previous datasets.

The normal-faulting mechanism of the off-Fukushima earthquake is similar to nearby shallow normal-faulting micro-seismicity within the overriding plate, with a tensile axis (σ_3) oriented in basically the east-west direction, which significantly increased after the Tohoku earthquake (Figures 1d–1f, e.g., Asano et al., 2011; Hardebeck & Okada, 2018; Hasegawa et al., 2012; Tanaka et al., 2014; Wang et al., 2019; Yoshida et al., 2012). This increase in the normal-faulting seismicity is considered to be related to the significant stress perturbation by the Tohoku earthquake, which switched the intraplate stress regime from horizontal compression to horizontal extension (e.g., Hasegawa et al. 2012). If we can obtain a detailed fault model of the off-Fukushima earthquake, then the quantitative relationship between the crustal stress released during the off-Fukushima earthquake and the stress increase due to the 2011 Tohoku earthquake can be discussed. This quantitative comparison will be useful to deepen our understanding of the temporal change of the crustal stress state associated with the Tohoku earthquake.

In the present study, we therefore estimate the detailed finite fault model of the off-Fukushima earthquake using the S-net OBPB data. From the finite fault model, we also attempt to examine the normal-faulting stress state within the crust around the off-Fukushima earthquake and its relationship with the Tohoku earthquake. The OBPB data process is described in Section 2, and Section 3 summarizes the feature in the S-net OBPB data. The spatial distribution of the initial sea surface height (tsunami source) and the finite fault model of the off-Fukushima earthquake are estimated in Sections 4 and 5, respectively. Section 6 examines the relationship between the Tohoku earthquake and the stress regime around the focal area. Section 7 concludes the present study.

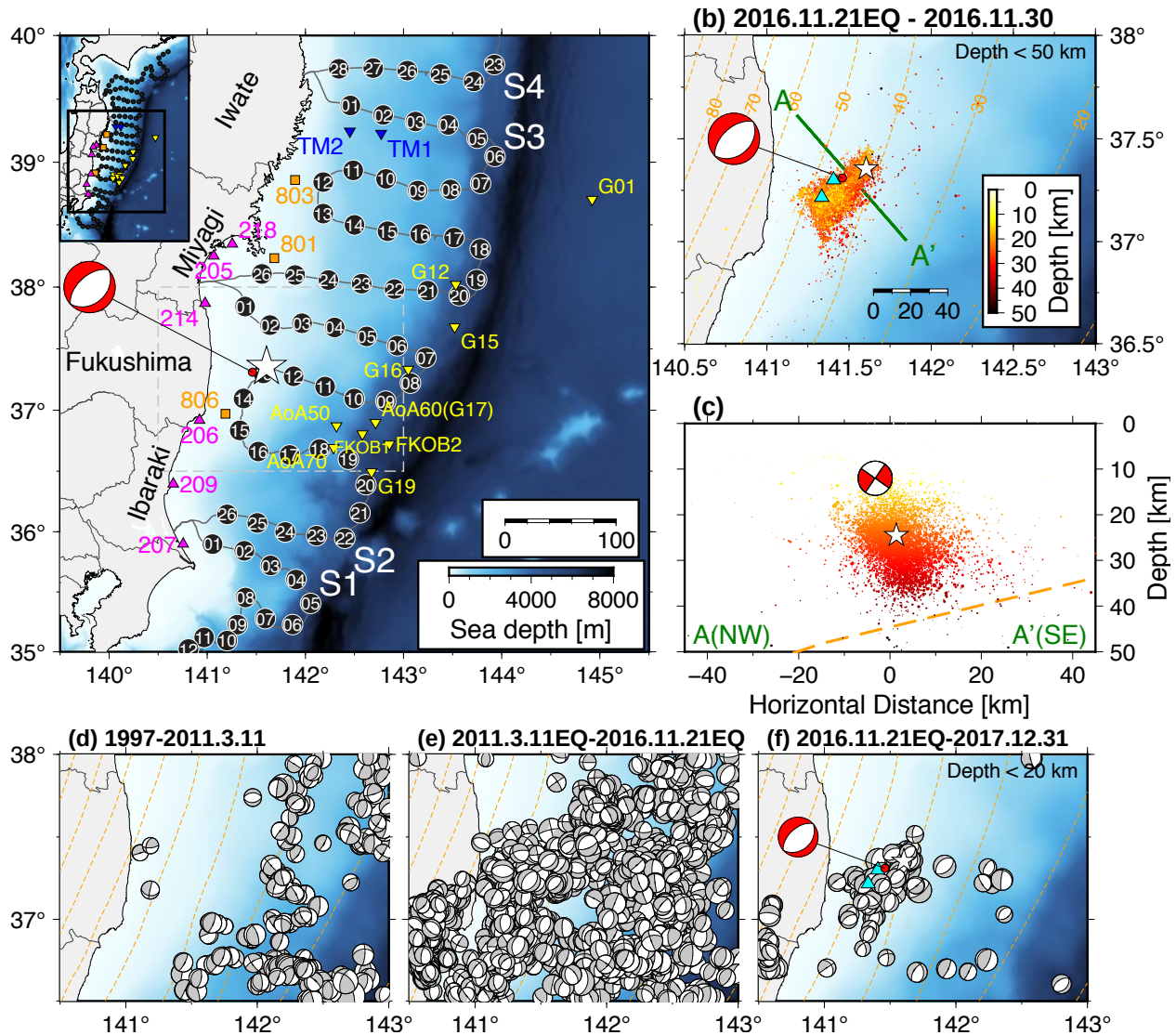


Figure 1. (a) Location map of the present study. Locations of the tsunami stations are shown by colored symbols (black circle: S-net OBP, blue inverted triangle: ERI OBP, yellow inverted triangle: Tohoku University OBP, orange square: NOWPHAS GPS buoy, pink triangle: NOWPHAS wave gauge). The epicenter (white star) and the CMT solution (red) of the off-Fukushima earthquake are taken from JMA and GCMT, respectively. (b) Enlarged view of the rectangular area drawn by gray lines in Figure 1a. Aftershocks during about one week as determined by JMA are shown (color denotes its depth). Orange contours show the depth of the subducting plate interface (Nakajima & Hasegawa, 2006). The locations of fresh seafloor cracks found by the JAMSTEC survey are shown by blue triangles. (c) Vertical cross section along line A-A' in Figure 1b. (d-f) The F-net fault mechanisms (Fukuyama et al., 1998) at depths shallower

than 20 km, (d) before the Tohoku earthquake, (e) during the Tohoku earthquake and the off-Fukushima earthquake, and (f) after the off-Fukushima earthquake.

2 Tsunami dataset

The present study used the S-net OBP data (black circles in Figure 1a), which was also used by Wang & Satake (2021). Although S-net now consists of 150 observatories (Aoi et al., 2020), 25 of these observatories, located at the outer-trench region, were not installed when the off-Fukushima earthquake occurred. Each observatory is equipped with absolute pressure sensors manufactured by Paroscientific, Inc. (e.g., Polster et al., 2009; Watts & Kontoyianiss, 1996). Two pressure sensors are equipped in each observatory for redundancy. The sensors are not directly exposed to the seawater, but rather are sealed in a metal housing filled with oil. The metal housing is further sealed in a metal cylindrical vessel filled with oil. The external pressure is transferred to the pressure sensor inside via a diaphragm made of hard rubber. See Aoi et al. (2020) for more details.

In addition to S-net, we use other OBPGs to evaluate the modeling resolution. We use the OBPGs off Iwate Prefecture installed by the Earthquake Research Institute (ERI) of the University of Tokyo (blue inverted triangles in Figure 1a, Gusman et al., 2017; Kanazawa & Hasegawa, 1997) and the OBPGs off eastern Japan installed by Tohoku University (yellow inverted triangles, Hino et al., 2014). We also use the offshore GPS buoys (orange squares) and wave gauges (pink triangles) of the Nationwide Ocean Wave information network for Ports and HARbourS [NOWPHAS] (Kawaguchi et al., 2017; Nagai et al., 1998).

3 Fundamental feature of the S-net OBPGs: Tsunami-irrelevant pressure signals

In order to investigate the fundamental feature of the S-net OBP data signals, we first process the OBP data. We decimate the original 10 Hz data to 1 Hz (Figure 2). We then subtract the theoretical tide calculated by the model of Matsumoto et al. (2000) and apply a low-pass filter with a cutoff of 100 s to reduce the high-frequency seismic wave signals (Figure 3).

Figure 2 shows the 1-Hz-sampling pressure waveforms. The high-frequency fluctuations related to the seismic waves and ocean-acoustic waves (e.g., Kubota, Saito, Chikasada et al., 2020) are observed. The gradual pressure increases related to the ocean tide are also observed, although some traces show different trends. The pressure changes recorded by the

two sensors equipped in the same observatory (black and gray lines) are very similar to each other. The difference between these two traces (red lines) is around zero, although some stations have offsets in the differences. At station S2N13, which is located just above the focal area of the off-Fukushima earthquake, no seismic or tsunamis signals were recorded.

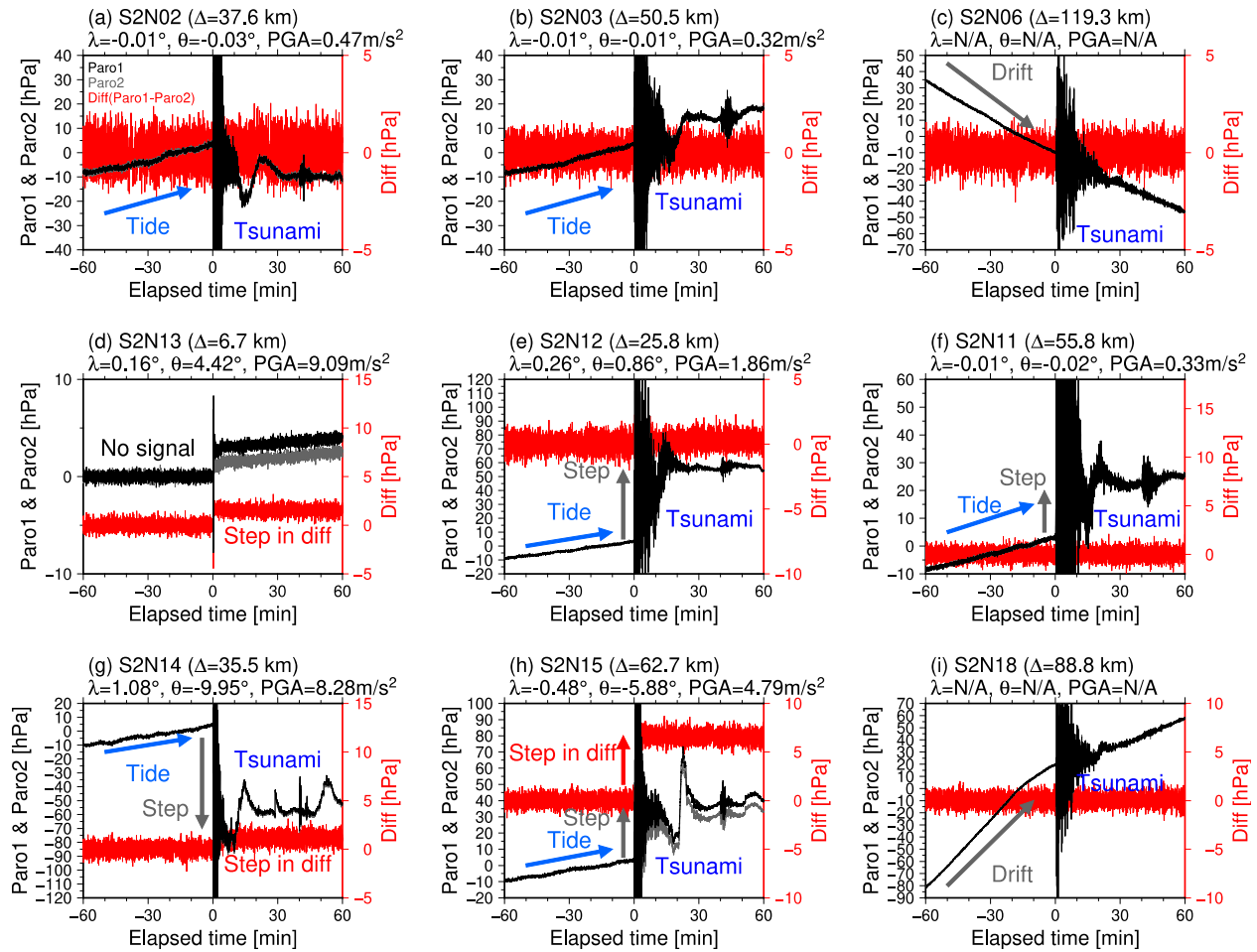


Figure 2. The 1-Hz ocean-bottom pressure waveforms for stations (a) S2N02, (b) S2N03, (c) S2N06, (d) S2N13, (e) S2N12, (f) S2N11, (g) S2N14, (h) S2N15, and (i) S2N18. Black and gray traces denote the waveforms from each of the pressure sensors. Red traces denote the difference between the two sensors. Note that the vertical scale for the difference waveforms is different in each subfigure. The dominant signals are indicated by arrows and text. The epicentral distance Δ measured from the JMA epicenter, and the tilt change λ , rotation angle change θ , and PGA values measured by the co-equipped accelerometer (Takagi et al., 2019) are also shown.

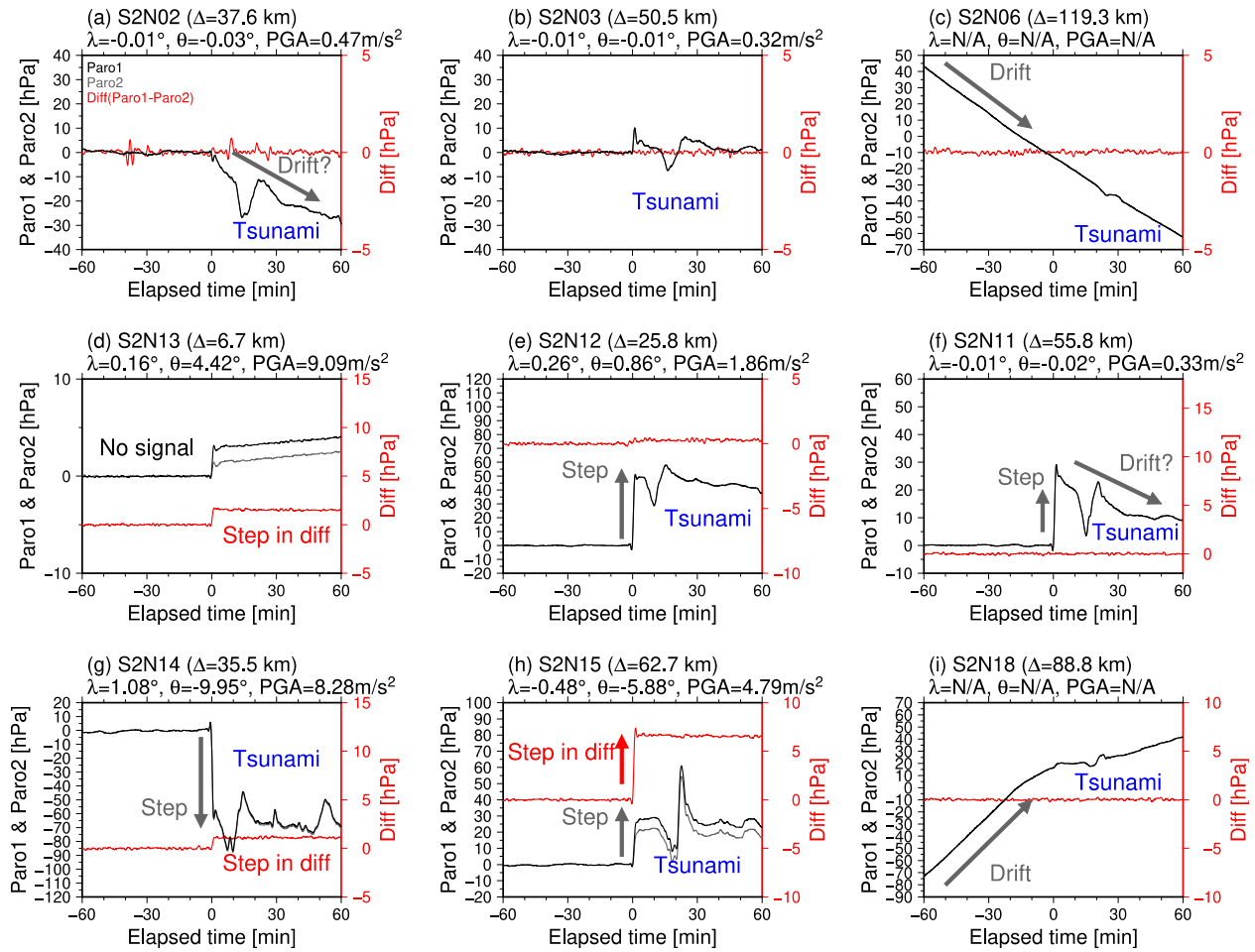


Figure 3. Ocean-bottom pressure waveforms after data processing for the stations. See Figure 2 for a detailed description.

Although the tsunamis are confirmed in the lowpass-filtered S-net OBPG waveforms (Figure 3), we also recognize some unfamiliar pressure signals irrelevant to the tsunamis, such as the large drift components (e.g., S2N06, S2N18). Since the observed drift rates are very large (e.g., ~ 50 hPa/hour at S2N06), these drifts are considered to be due to neither tsunamis nor postseismic seafloor deformations. It might be possible that the mechanical drifts of the pressure sensors are the cause of these drifts, because it was reported that the Paroscientific pressure sensors contain instrumental drift with rates of ~ 8.8 hPa/year (Inazu & Hino, 2011; Polster et al. 2009; Watts & Kontoyianiss, 1996). However, the previously-reported drift rates of the Paroscientific pressure sensors are much smaller than those confirmed in the S-net. In addition, it is incomprehensible that the drift rates are completely identical in the sensor pair, although the drift rates must be different in each sensor. Therefore, we do not consider the cause of these

drifts to be as previously reported. Although we cannot identify the reason for these drifts, we suspect the observation system of the S-net may be related to the cause of the drift.

In addition, abrupt steps at the origin time are observed at some OBPGs, particularly at S2N11, S2N12, S2N14, and S2N15. The step is also observed at S2N13, where no tsunami signals were recorded (Figure 3d). If we consider the pressure offset changes as a result of the seafloor vertical movement, these pressure changes correspond to a seafloor vertical displacement of ~30–60 cm (assuming a pressure change of 1 hPa is equal to a seawater column height change of 1 cm H₂O). Considering the source-station distances, these displacements seem too large compared with those expected from typical M~7 earthquakes. Furthermore, even if the OBPGs are located inside the focal area where the vertical displacement is large, the ocean-bottom pressure, or the seawater column height above the OBPG, cannot change so abruptly because both seafloor and sea-surface simultaneously move vertically during tsunami generation (e.g., Tsushima et al. 2012). Therefore, these steps are unlikely to be caused by the seafloor permanent displacement. Similar pressure steps were also recorded by the S-net and the other OBPG networks during the past earthquakes (Kubota, Suzuki et al., 2018; Kubota, Saito, Suzuki, 2020; Wallace et al. 2016), which are not considered to be related to the tsunami or the seafloor crustal deformation.

It has been reported that outputs of Paroscientific pressure sensors strongly depend on its orientation relative to the direction of gravity (Chadwick et al., 2006). Thus, the step signals might be caused by the rotation of the pressure sensor. According to Chadwick et al. (2006), the rotation angle change of the pressure sensor of $\theta \sim 10^\circ$ roughly corresponds to the apparent pressure offset change of up to ~10 hPa. Takagi et al. (2019) analyzed the co-equipped accelerometer during the off-Fukushima earthquake and found that some observatories near the epicenter rotated associated with large seafloor ground motion (Figures 2 and 3). However, comparing the rotation angles at some near-source stations (e.g., $\theta = 0.86^\circ$ at S2N12 and 9.95° at S2N14, Takagi et al., 2019), the observed pressure steps were extremely large ($> \sim 50$ hPa). Furthermore, considering that the sensitivity to the rotation angle must be different in each sensor, it is quite strange that the amounts of the pressure step in two pressure sensors are almost identical. We also confirm that the pressure steps in the two pressure sensors are different at some stations where the large rotation was observed (e.g., S2N13, S2N15), leading to the steps around the focal time in the difference traces between the two sensor outputs (red lines in Figure

3). Taking these points into account, we consider that the dominant cause of the pressure steps is not the response to the sensor rotation, as reported by Chadwick et al. (2006), but might be the observation system of the S-net, and the difference in the steps between the two sensors may be due to the difference in the response to the rotation angle. As a summary of this section, we emphasize that we must be careful to analyze the OBPG data to distinguish whether such signals are real or are artifacts related to the drift or offset, although the S-net OBPGs clearly recorded the tsunamis due to the 2016 off-Fukushima earthquake.

4 Tsunami source modeling

4.1 Modeling procedure

In this section, we analyze the S-net data to estimate the spatial distribution of initial sea-surface height (tsunami source) of the off-Fukushima earthquake and to investigate how the S-net OBPGs provide better constraint. In order to reduce the long-period tsunami-irrelevant drift signals as well as the short-period seismic wave components, we apply the bandpass filter with passbands of 100–3,600 s (Figure 4b). We here briefly describe the procedure for the tsunami source modeling. The full details are shown in Text S1.

We set the analytical area as 50 km × 50 km (rectangular area in Figure 4a) and distribute the unit source elements of the seafloor vertical displacement with horizontal spatial intervals of 2 km. Assuming that the seafloor displacement from the unit source elements is equivalent to the initial sea-surface height change, we simulate a tsunami by solving a linear dispersive tsunami equation (Saito, 2019; Saito et al., 2010). We use the JTOPO30 bathymetry data with a spatial resolution of 30 arcsec (<http://www.mirc.jha.jp/en/>), interpolating the spatial interval of $\Delta x = \Delta y = 1$ km. The displacement is assumed to occur instantaneously at time $t = 0$ s. After calculation, the pressure offset change due to the seafloor displacement is subtracted from the sea-surface height change assuming that a sea height change of 1 cm H₂O is equal to a pressure change of 1 hPa (the method of Tsushima et al., 2012). We finally apply the same bandpass filter to the simulated waveform as that applied to the observation.

In the inversion analysis, we use the time-derivative waveforms for the inversion analysis ($\partial p / \partial t$, the method of Kubota, Suzuki et al. (2018)), because the time-derivative can reduce the artificials due to the tsunami-irrelevant steps, which becomes the impulse and thus does not contain the offset change. The data time window used for the modeling is manually

determined, which includes the main part of the tsunami (indicated by the blue traces in Figure 4c). The goodness of the estimated source is evaluated using the variance reduction (VR):

$$VR = \left(1 - \frac{\sum_i (d_i^{obs} - d_i^{cal})^2}{\sum_i d_i^{obs2}} \right) \times 100 (\%) \quad (1)$$

where d_i^{obs} and d_i^{cal} are the i -th data of the observed and calculated time-derivative pressure waveforms. We impose the smoothing constraint for the inversion, and its weight is determined based on the trade-off between the weight and the VR (Figure S1) to avoid both the overfitting and oversmoothing of data.

4.2 Results

Figure 4 shows the results of the inversion. A subsidence with a horizontal extent of $\sim 40 \text{ km} \times \sim 20 \text{ km}$, having a sharp peak near the GCMT centroid, was obtained (Figure 4a). The direction of the northeast-southwest extents of the subsided region is consistent with the GCMT strike angle of 49° . The northwest edge of the subsidence region is consistent with the locations where the seafloor displacements of 1–2 m and fresh seafloor cracks were found by a seafloor bathymetry survey just after the off-Fukushima earthquake conducted by Japan Agency for Marine-Earth Science and Technology [JAMSTEC] (blue triangles in Figure 4a). The time derivatives of the S-net pressure waveforms were well reproduced ($VR = 95.7\%$, Figure 4c). Except for the waveforms just after the focal time at some near-source OBPGs, the observed pressure is also well explained (Figure 4b). The waveforms recorded at the other tsunami stations (Figure 1a) are also reproduced surprisingly well (Figure 5), even though they were not used for the inversion. This suggests that the use of the S-net tsunami data provides good spatial resolution of the tsunami source, and thus it is expected that we can obtain a reliable fault model. Note that the later arrivals in some stations (e.g., $\sim 100 \text{ min}$ at TM1 and TM2) are not well reproduced, which are caused by the coastal-reflections (Gusman et al., 2017). This is probably because the spatial resolution of the coastal shape from the topography data in our simulation is

not sufficient ($\Delta x = \Delta y = 1$ km) to reproduce the reflected tsunami waves, and the high-resolution bathymetry data is important to reproduce the reflected tsunamis (Gusman et al., 2017; Kubota, Saito et al., 2018).

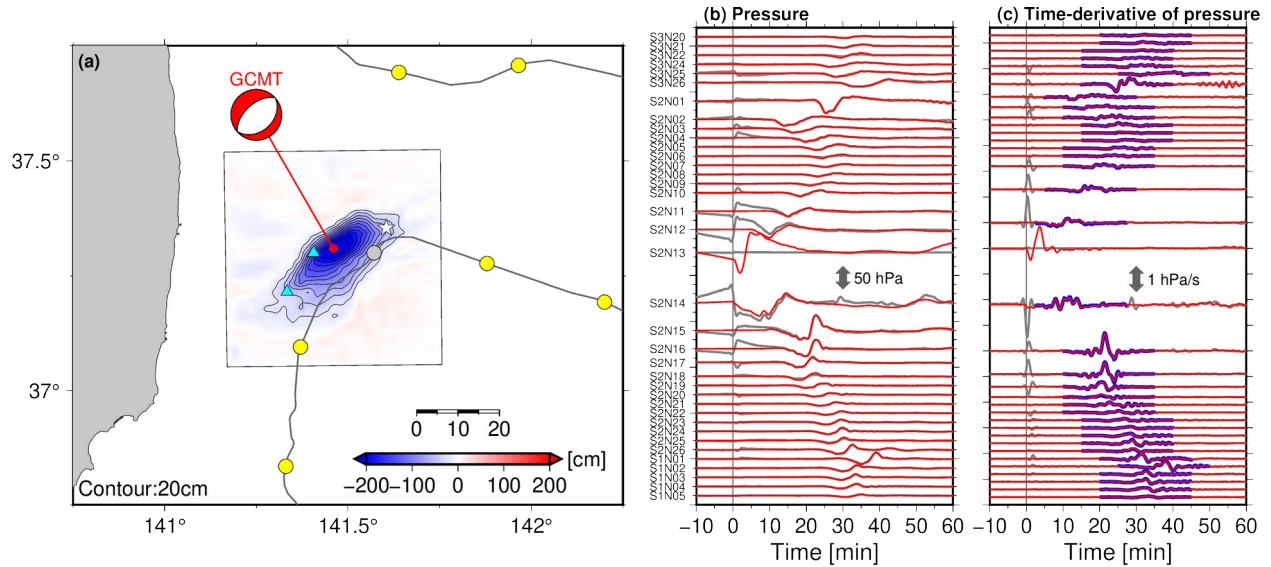


Figure 4. Results of the tsunami source inversion. (a) Spatial distribution of the tsunami source. Contour lines denote the subsided region with intervals of 20 cm. The white star is the JMA epicenter, and blue triangles denote the location of the seafloor survey, where fresh surface cracks were found. The yellow and gray circles show the S-net OBPB locations used or not used, respectively, for inversion analysis. Comparisons of (b) the pressure waveforms and (c) the time-derivative waveforms. The gray and red traces denote the observed waveforms and simulated waveforms from the tsunami source model. Traces marked by blue lines denote the time window used for the inversion analysis.

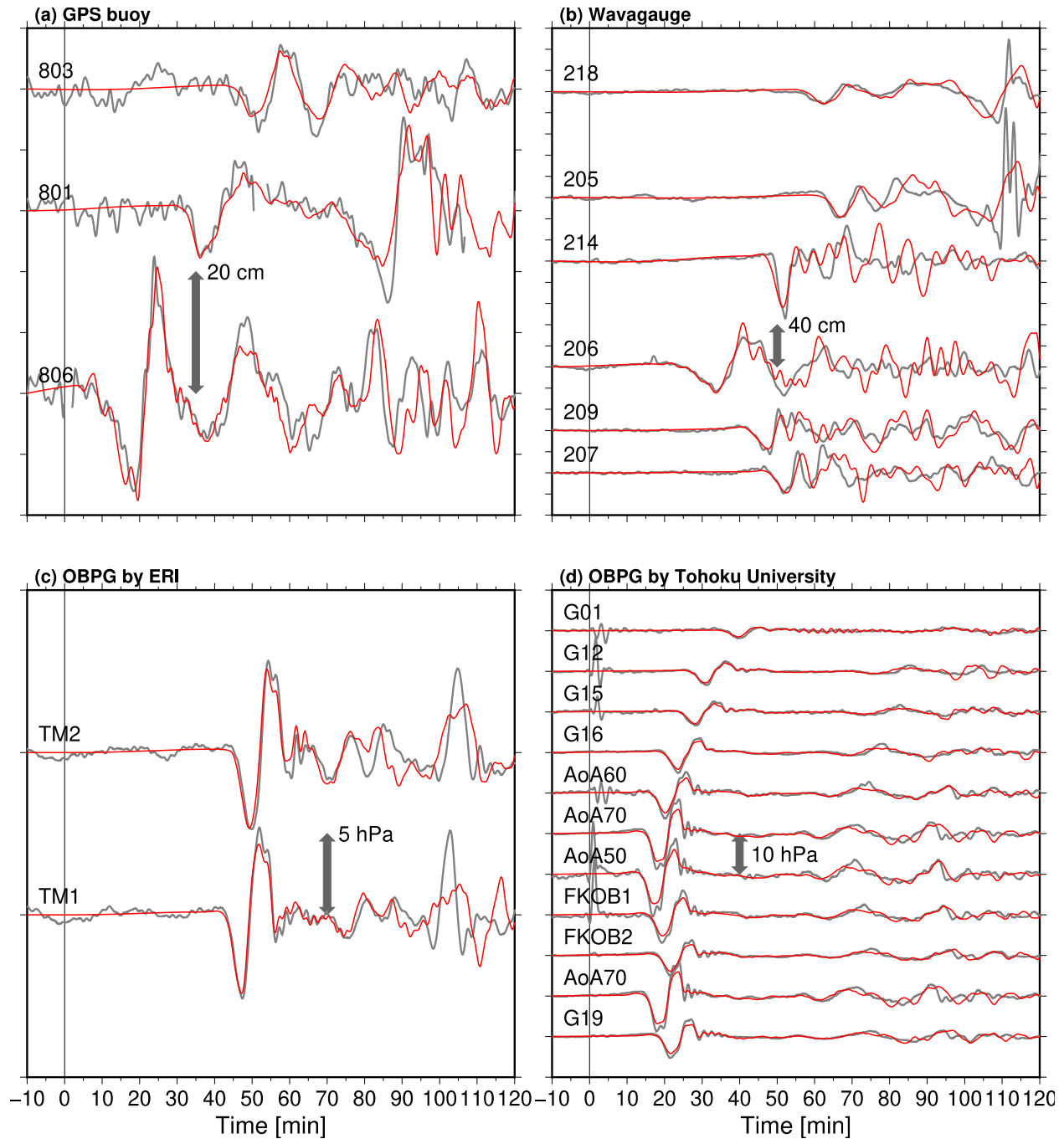


Figure 5. Waveform comparisons for the other tsunami stations, from the tsunami source model, for (a) NOWPHAS Near-coastal GPS buoys, (b) NOWPHAS wave gauges, (c) OBPGs installed by ERI, and (d) OBPGs installed by Tohoku University. At station 801, the waveforms during the data missing are not drawn. See Figure 1 for station locations.

296 In the inversion, we used the time-derivative waveforms of the pressure to reduce the
297 artificials attributed to the tsunami-irrelevant pressure components (Kubota, Suzuki et al., 2018).
298 In order to see how well this method reduced the artificials, we also conduct the additional
299 inversion using the original pressure waveforms, instead of its time-derivative waveforms
300 (Figure S2). The weight of the smoothing is also determined based on the VR between the
301 observed and simulated pressure waveforms (Figure S1). As a result, the distribution of the
302 tsunami source is fundamentally similar to the original distribution, although a significant
303 artificial uplift of > 60 cm is estimated around S2N14 where the large step was recorded. In order
304 to avoid this artificial due to the tsunami-irrelevant components, using the inversion method by
305 time-derivative waveforms (Kubota, Suzuki et al., 2018) worked very well to reduce the artificial
306 due to the apparent step signals irrelevant to the tsunami or the seafloor displacement.

307 We compare the tsunami source model estimated by the present study with the models
308 obtained using the tsunami data, except for the S-net data, by Gusman et al. (2017) (Figure 6a),
309 Adriano et al. (2018) (Figure 6b), and Nakata et al. (2019) (Figure 6c). The horizontal location
310 and spatial extent of the subsided region of our tsunami source model roughly correspond to
311 those obtained by the previous studies. However, the amount of the maximum subsidence was
312 much larger than the previous models and the locations of the peak subsidence of tsunami source
313 are slightly different from each other. Our tsunami source model had a maximum subsidence of
314 ~ 238 cm, whereas the two models obtained from the far-field tsunami data (Gusman et al. 2017;
315 Adriano et al., 2018) underestimated the subsidence (~ 180 cm and ~ 130 cm, respectively, Table
316 1). The subsidence peak of our model was located ~ 5 – 10 km southeast of the models by Gusman
317 et al. (2017) and Nakata et al. (2019) and ~ 10 km east of the model by Adriano et al. (2018). One
318 reason for these differences may be the assumption of the fault geometry, but the more
319 significant reason should be the station coverage and the source-station distance. The coastal tide
320 gauges or the offshore stations used in these previous studies were located far from the source
321 region and the stations at the offshore side of the source region were not used in these studies,
322 whereas the S-net has better station coverage and a smaller source-station distance. This could
323 provide a better constraint on the horizontal location and peak displacement amount to reproduce
324 surprisingly well the tsunami waveforms not used for the inversion. Thanks to this improvement
325 in the constraint, we believe that we can obtain a finite fault model with a higher resolution, as
326 shown in the next section.

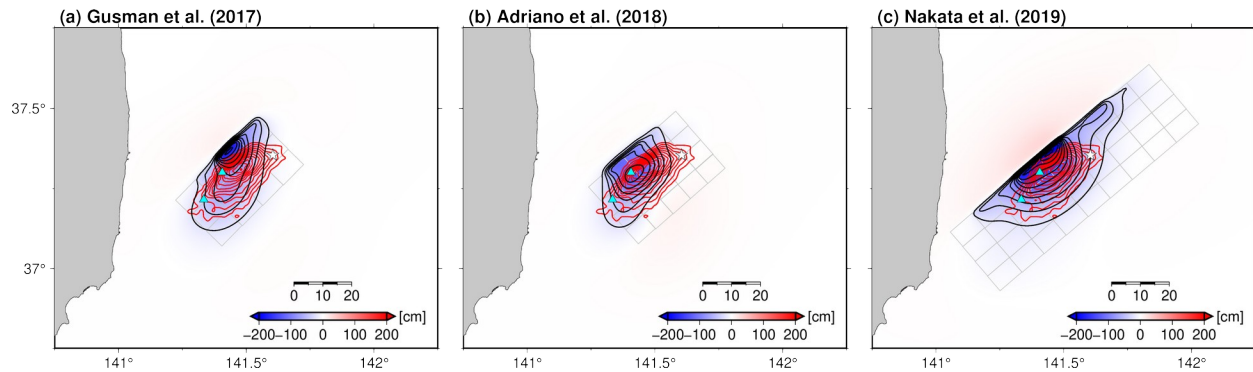


Figure 6. Comparison of the tsunami source calculated from the finite fault models of the previous studies (black contours) and the tsunami source model (red). Models of (a) Gusman et al. (2017), (b) Adriano et al. (2018), and (c) Nakata et al. (2019) are shown. The contour intervals are 20 cm. The configuration of the fault is also shown by gray lines.

5 Fault modeling

5.1 Rectangular fault model with uniform slip

Here, we attempt to constrain the finite fault model of the off-Fukushima earthquake. The horizontal location and the peak subsidence of our tsunami source distribution are slightly different from the other previous models. Therefore, we first constrained the optimum fault location based on a grid-search approach (Kubota et al., 2015; 2019). In the grid-search, we assume one planar rectangular fault with a uniform slip. The strike angle of the fault is fixed to the GCMT value (strike = 49°), considering the consistency with the direction of the northeast-southwest extent of the tsunami source. Since the dip and rake angles cannot be constrained only from the tsunami source, we assume these angles based on the GCMT solution (dip = 35° and rake = -89°), as inferred from the analysis of the teleseismic data. To find the optimum model that best reproduces the S-net waveforms, we vary the other fault parameters and simulate tsunamis. The unknown parameters of the rectangular fault that we search are the fault center location (longitude, latitude, and depth) and its dimensions (length L and width W). The slip amount on fault D is adjusted to maximize the VR in Eq. (4). The search range for these parameters is summarized in Table S1, which is determined based on the tsunami source model obtained in the previous section. Using an assumed rectangular fault with a set of parameters (the

351 fault model candidate), we calculated the seafloor displacement (Okada, 1992) and simulated the
352 tsunamis. The goodness of each of the fault model candidates is evaluated using the VR values.

353 The horizontal location of the optimum fault is shown in Figure 7a. The detailed
354 results of the grid-search analysis are shown in Figure S3. We obtain the optimum fault model as
355 $L = 15$ km, $W = 10$ km, and $D = 467.7$ cm ($M_0 = 2.1 \times 10^{19}$ Nm, M_w 6.8, assuming a rigidity of μ
356 $= 30$ GPa). The center of this model is located at a depth of 10 km, ~ 10 km east of the GCMT
357 centroid (the detailed parameters are listed in Table 1). The GCMT centroid depth was 12 km
358 and the aftershocks are mainly located at depths of ~ 20 km (Figures 1b and 1c), whereas the
359 estimated fault is located at the very shallow part of the crust (Figure 1c and Table 1). This
360 disagreement has also been pointed out by Gusman et al. (2017) from their numerical
361 simulations. They suggested that the aftershocks determined from the inland network are
362 systematically deeper than the actual depth. The horizontal extent of the tsunami source is
363 relatively narrow and is located at the northeast, compared with that obtained by the inversion
364 analysis (Figures 7a and S3a). The reproductivity of the S-net pressure waveforms is reasonable
365 (Figures S3b and S3c), although the VR is lower than that for the tsunami source inversion
366 ($VR_{\text{optimum}} = 59.3\%$). These mismatches are probably because of the simple assumption of the
367 rectangular fault, which could not reproduce the southwest part of the tsunami source.

368

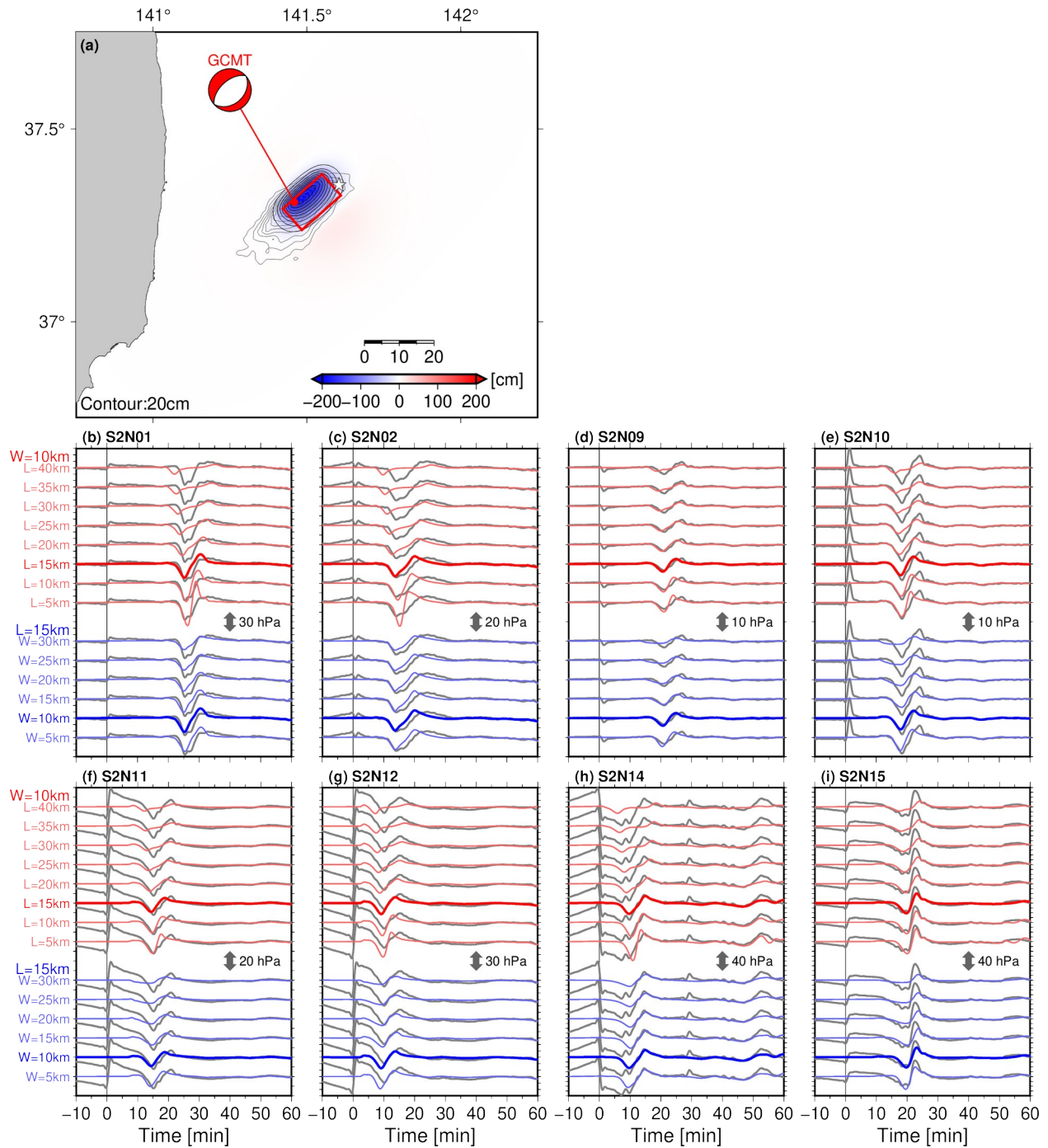


Figure 7. (a) Horizontal location of the optimum rectangular fault model. The red rectangle shows the location of the rectangular fault model. (b–i) Evaluation of the fault dimension. Comparisons of the stations near the epicenter between the observed (gray) waveform and the simulated waveforms from the varied fault dimensions are shown. The simulated waveforms with thick red and blue traces denote the optimum rectangular fault.

If we consider the empirical scaling relations from the magnitude, then the fault dimension is expected to be $\sim 700 \text{ km}^2$ (e.g., Wells & Coppersmith, 1994). On the other hand, the estimated fault dimension of 150 km^2 is much smaller. In order to assess the dimensions of the rectangular fault, we simulate tsunamis, fixing the seismic moment M_0 and the fault center location to the optimum model and varying the fault dimensions. In Figures 7b to 7i, we compare the waveforms of representative S-net stations relatively close to the focal area. If we assume a larger fault with $L > 20 \text{ km}$, then the arrival of the peak downheaval wave and its amplitude cannot be explained for the stations located northward (S2N01 and S2N02) or southward (S2N14 and S2N15) from the source. In addition, the sharp peak of the downheaval waves observed at the stations located eastward (S2N09, S2N10, S2N11, S2N12, and S2N15) from the source are not well reproduced by the fault width for the case in which $W > 15 \text{ km}$. These results suggest that the fault dimensions should be $L \leq \sim 20 \text{ km}$ and $W \leq \sim 15 \text{ km}$. Considering this range, the estimated fault dimensions are obviously smaller than expected based on the scaling relation. These much smaller fault dimensions are consistent with the size of the asperity, defined as the region of the large slip on the fault (e.g., Somerville et al., 1999), expected from the empirical relation deduced from the inland crustal earthquakes (Somerville et al., 1999; Miyakoshi et al., 2020). This may suggest that this optimum rectangular fault corresponds to the asperity.

5.2 Slip distribution

We then conduct a finite fault inversion to estimate the slip distribution (finite fault model) in a similar manner to that reported by Kubota, Saito et al. (2018). We assume a rectangular planar fault with dimensions of $45 \text{ km} \times 30 \text{ km}$, so that the fault passes through the optimum fault obtained by the grid search. The planar fault is divided into subfaults with size $3 \text{ km} \times 3 \text{ km}$. We then simulate the Green's function, i.e., the pressure change waveforms excited by each subfault, using a similar calculation procedure to that used in the grid-search analysis. The inversion scheme is almost the same as the tsunami source inversion analysis, but we imposed a nonnegativity constraint (Lawson & Hanson, 1974). The weighting of the smoothing constraint is determined by trial and error.

The slip distribution obtained by the inversion analysis and the tsunami source distribution calculated from this slip distribution are shown in Figure 8a. The tsunami source distribution is similar to that obtained by the tsunami source inversion (Figure 4).

The S-net and other tsunamis waveforms are well explained ($VR = 72.4\%$, Figures S4b, S4c, and S5). We obtain a maximum slip of $D_{\max} = 637.2$ cm, and the total seismic moment is $M_0 = 6.3 \times 10^{19}$ Nm ($M_w 7.1$, $\mu = 30$ GPa). The large slip is concentrated in the northeastern part of the fault plane, corresponding to the rectangular fault estimated by the grid-search analysis. More specifically, subfaults with slip amounts with $D > 0.5 \times D_{\max}$ roughly correspond to the rectangular fault (subfaults marked by green lines in Figure 8a, 41% of the total M_0 , $M_w 6.9$). In addition, a relatively small slip also extends to the southwestern part, which was not resolved in the grid-search analysis. The reason why this slip was not resolved in the grid search is probably the simple assumption of the uniform slip rectangular fault. If we take subfaults with slip amounts larger than $0.2 \times D_{\max}$, then both large northeastern slip and relatively small southwestern slip are included (indicated by the thick black lines in Figure 8). Thus, we define these subfaults as the rupture area. The rupture area had dimensions of ~ 30 km \times ~ 20 km, and 81% of the total moment was concentrated in the main rupture area. The horizontal location of the centroid, defined as the slip-weighted average of subfaults within the rupture area (pink star in Figure 8a, Table 1), is located ~ 5 km southeast from the GCMT centroid.

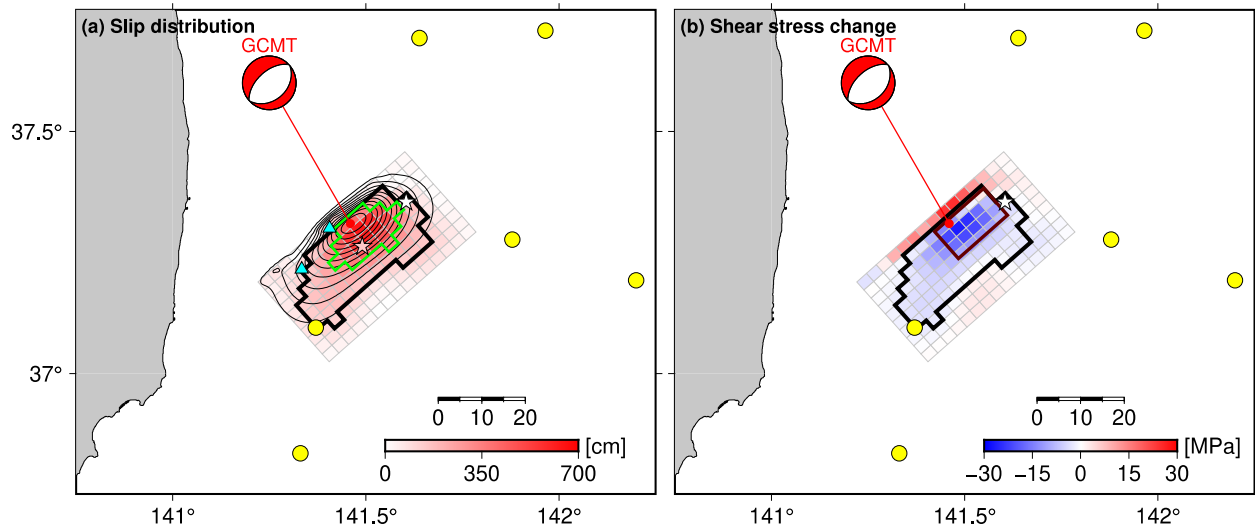


Figure 8. Result of the slip inversion. (a) Slip distribution (colored tiles) and tsunami source distribution (black contours, 20 cm interval). The pink and white stars indicate the slip-weighted averaged centroid and the JMA epicenter, respectively. Subfaults with slip amounts larger than $0.2 \times D_{\max}$ and larger than $0.5 \times D_{\max}$ are marked by thick black lines and green lines, respectively. (b) Shear stress change along the fault. Negative (blue) and positive (red) denote

the shear stress decrease and increase, respectively. The dark red rectangle denotes the optimum rectangular fault obtained by the grid-search analysis.

In Figure 8b, we calculate the distribution of the shear stress change along the fault, using the equation of Okada (1992). The rectangular fault estimated by the grid-search analysis agrees well with the region where the shear stress is largely released (green rectangle in Figure 8b), indicating that the rectangular fault model corresponds to the asperity, as discussed above. Using the shear stress change distribution, we calculate the energy-based stress drop $\Delta\sigma_E$ (Noda et al., 2013) as:

$$\Delta\sigma_E = \frac{\sum_i D_i \Delta\sigma_i}{\sum_i D_i}, \quad (7)$$

where D_i is the slip amount at the i -th subfault, and $\Delta\sigma_i$ is the stress drop at the i -th fault, which is defined as the shear stress change (Figure 8b) multiplied by -1 . Using the subfaults within the rupture area, we obtain $\Delta\sigma_E = 10.0$ MPa. This stress drop seems not so small as expected for the interplate earthquakes (an order of $\sim 10^0$ MPa, e.g., Kanamori & Anderson 1975), but rather is consistent with the intraplate earthquakes, which generally have stress drop values of $\sim 10^1$ MPa (e.g., Somerville et al., 1999; Miyakoshi et al., 2020).

6. Discussion: implication for the intraplate stress regime

After the 2011 Tohoku earthquake, it has been reported that the normal-faulting seismicity significantly increased in the upper plate, which is thought to be related to the stress perturbation by the Tohoku earthquake (Figures 1d–1f, Asano et al., 2011; Hasegawa et al., 2012; Yoshida et al., 2012). The 2016 off-Fukushima earthquake is also considered to be an event of the normal-faulting seismicity related to the stress perturbation by the Tohoku earthquake. This change in seismicity is interpreted as the result whereby the intraplate stress regime switched after the Tohoku earthquake from the horizontal compression to the horizontal extension (e.g., Hasegawa et al. 2012). As discussed previously, the use of the S-net tsunami data

improved the constraint on the tsunami source and the fault model of the off-Fukushima earthquake, which made it possible to obtain the detailed distribution of the shear stress reduction and the static stress drop. Using these results, we attempt to discuss the quantitative relationship between the crustal stress released during the off-Fukushima earthquake and the stress increase due to the 2011 Tohoku earthquake. This kind of discussion is typically difficult to conduct because it is rare that both the high-resolution fault model of the M~7 offshore earthquake and the significant stress perturbation due to the megathrust earthquake are available.

If the stress regime switched by the Tohoku earthquake in the vicinity of the off-Fukushima earthquake, the deviatoric stress, or the initial shear stress on the fault of the off-Fukushima earthquake, should be smaller than (or at least equivalent to) the static shear stress increase due to the Tohoku earthquake (Figure 9a). In other words, the stress drop of the off-Fukushima earthquake should be smaller than the shear stress increase due to the Tohoku earthquake. In Figure 10a, we calculate the shear stress change due to the Tohoku earthquake, using the fault model of Iinuma et al. (2012), along the fault geometry of the off-Fukushima earthquake. The shear stress change related to the Tohoku earthquake around the focal area of the off-Fukushima earthquake is only ~2 MPa, which is smaller than the stress drop of the off-Fukushima earthquake. The larger stress drop of the off-Fukushima earthquake than the stress increase after the Tohoku earthquake is inconsistent with the presumption that the intraplate stress regime switched by the static stress change of the Tohoku earthquake. There should be other causes for the normal-faulting stress regime around the focal area of the off-Fukushima earthquake.

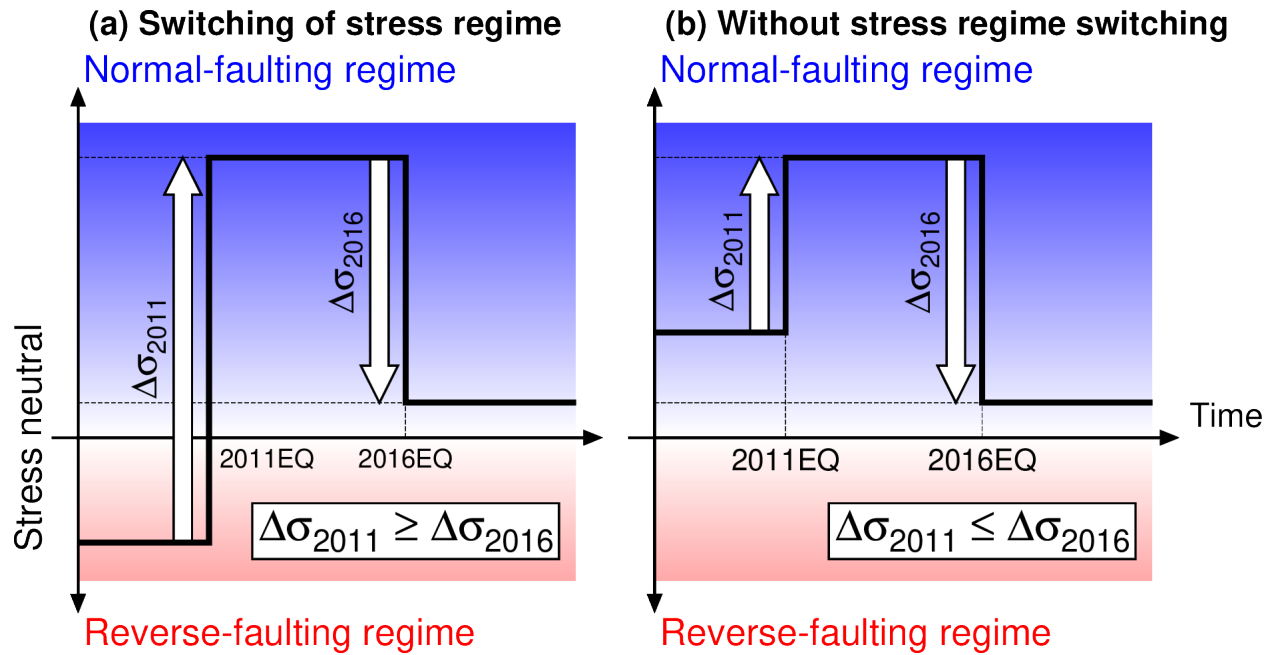


Figure 9. Schematic illustration of the temporal change of the stress regime around the off-Fukushima earthquake. The stress regimes (a) assuming the switching of the stress regime after the Tohoku earthquake and (b) without assuming the stress switching.

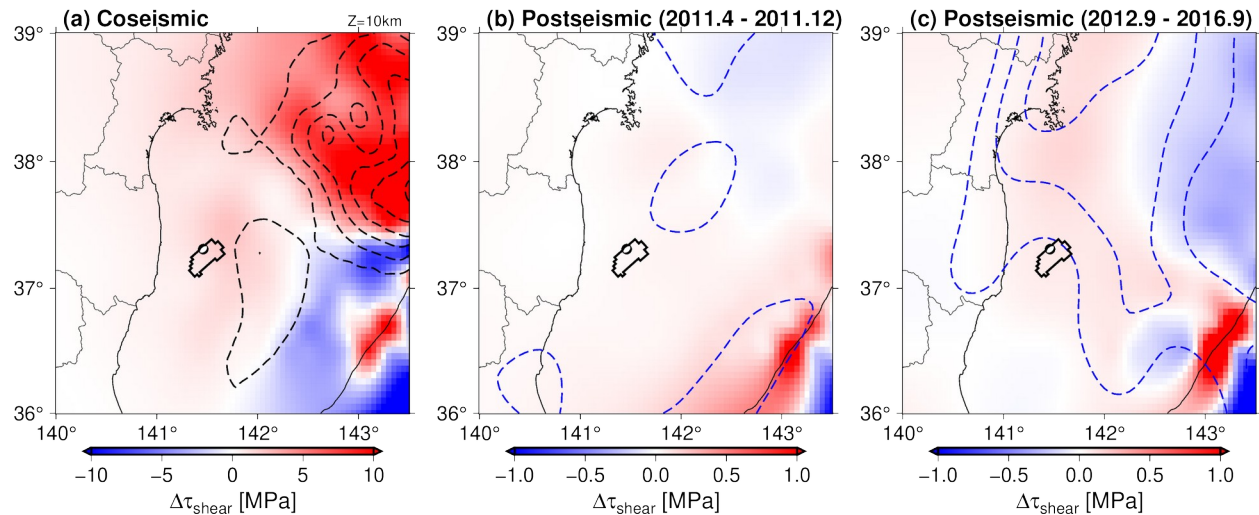


Figure 10. Horizontal distribution of the shear stress change on the 2016 off-Fukushima earthquake fault at a depth of 10 km. Shear stress changes along the fault geometry of the off-Fukushima earthquake due to (a) the Tohoku earthquake (Iinuma et al. 2012), (b) postseismic slip during April 2011 and December 2011 (Iinuma et al., 2016), and (c) Postseismic slip during September 2012 and September 2016 (Tomita et al. 2020). The main rupture area of the 2016

off-Fukushima earthquake inferred from the inversion analysis is also indicated by black lines.
Note that the color scales are different in each subfigure.

One possible cause is the postseismic slip of the Tohoku earthquake (Iinuma et al., 2016; Tomita et al., 2020). After the Tohoku earthquake, the postseismic seafloor deformation was detected by the seafloor geodetic observation (Tomita et al., 2015; 2017), which was caused by the postseismic slip along the fault and the viscoelastic deformation (Sun et al., 2014; Iinuma et al., 2016; Tomita et al., 2020). Among the postseismic deformation, the afterslip along the plate interface is dominant in the south of the rupture area of the Tohoku earthquake, including the region off Fukushima, whereas the viscoelastic deformation dominates the northern part of the Tohoku earthquake rupture area (Iinuma et al., 2016; Tomita et al., 2020). Therefore, we calculate the shear stress change on the 2016 fault geometry using the postseismic slip models to evaluate the contribution by the postseismic slip around the focal area. We calculate the stress change using the postseismic slip model from 23 April 2011 to 10 December 2011 proposed by Iinuma et al. (2016) (Figure 10b). The calculated shear stress change is too small (on the order of 10^{-1} hPa) to complement the shortage of the stress change of the off-Fukushima earthquake. We also calculated the stress change using the postseismic slip model during 2012 and 2016 (Tomita et al., 2020) and found that its contribution was also minor (Figure 10c). We therefore concluded that the shear stress increase due to the postseismic slip could not resolve the apparent contradiction between the stress drop of the off-Fukushima earthquake and the shear stress increase after the Tohoku earthquake. This contradiction arose from the assumption of the switching of the stress regime, which was a reverse-faulting and a normal-faulting regime before and after the Tohoku earthquake, respectively.

It was thought that the horizontal compressive stress attributed to the plate coupling force was widely dominant in Japan before the Tohoku earthquake (e.g., Wang & Suyehiro, 1999; Terakawa & Matsu'ura, 2010). However, there are some recent reports that some normal-faulting microearthquakes occurred even before the Tohoku earthquake in the inland region of Fukushima prefecture (Imanishi et al., 2012; Yoshida et al., 2015a; 2015b). This normal-faulting seismicity was interpreted as a result of the normal-faulting stress regime being predominant in this location even before the Tohoku earthquake. One possible reason for this normal-faulting stress regime is the effect of bending of the overriding plate, in which the horizontal extensional

and compressional stresses develop at the shallower and the deeper portion of the plate, respectively (e.g., Turcotte & Schubert, 2002; Hashimoto & Matsu'ura 2006; Fukahata & Matsu'ura, 2016). Yoshida et al. (2015a) showed that the normal-faulting stress regime is dominant at depths shallower than ~ 15 km in this region, while the reverse-faulting stress regime is dominant at depths greater than ~ 15 km, which is consistent with the hypothesis. We can also consider the topographic effects (Wang et al., 2019) for the formation of the horizontal extensional stress. Taking these past studies into account, it is reasonable to interpret this apparent contradiction, in which the stress perturbation by the Tohoku earthquake around the off-Fukushima earthquake is insufficient to switch the intraplate stress regime, that the horizontal extensional stress regime was already predominant around the 2016 off-Fukushima earthquake even before the Tohoku earthquake (Figure 9b).

Some major normal-faulting earthquakes were reported around the focal area of the off-Fukushima earthquake in 1938 (Abe, 1977; Murotani, 2018). Furthermore, according to the geologic cross-section around the off-Iwaki gas field, which is located near the 2016 off-Fukushima earthquake, the northeast-southwest-trending reverse faults were developed at a depth shallower than 6 km, which are considered to have formed during Oligocene and Miocene (Iwata et al., 2002). Along this fault trace, it was also reported that the normal-faulting-type surface offsets with vertical offset of 5–10 m were found, and it was suggested that the direction of the tectonic stress flipped to the normal-faulting regime during Quaternary and a normal-faulting earthquake similar to the 2016 off-Fukushima earthquake repeatedly occurred along this fault (S. Toda, https://irides.tohoku.ac.jp/media/files/earthquake/eq/2016_fukushima_eq/20161122_fukushima_eq_activefault_toda.pdf, in Japanese). These reports may support our hypothesis that the crustal stress regime was under the normal-faulting regime even before the Tohoku earthquake.

Note that the downdip limit of the main rupture area of our fault model the off-Fukushima earthquake is ~ 14 km, which is approximately consistent with the downdip limit depth of the normal-faulting regime in the inland Fukushima region estimated by Yoshida et al. (2015a). This suggests that the horizontal extensional stress regime before the Tohoku earthquake around the focal area of the off-Fukushima earthquake is predominant at depths shallower than 15 km and the stress neutral zone related to bending of the overriding plate lies at a depth of ~ 15 km. We also note that the normal-faulting seismicity extensively increased in the

overriding plate, even at a depth deeper than 15 km (e.g., Asano et al., 2011; Hasegawa et al., 2012). This might suggest that the stress-neutral depth was slightly deepened around this region after the Tohoku earthquake.

As a summary of this discussion, the temporal change of the intraplate crustal stress around the off-Fukushima earthquake can be interpreted as follows. The horizontal extensional stress was predominant before the Tohoku earthquake within the shallowest part of the continental plate, but may not exceed the crustal strength. After the Tohoku earthquake, its stress perturbation enhanced the extensional stress, provoking the normal-faulting seismicity.

Before the 2011 Tohoku earthquake, no major seismicity was detected around the focal area of the off-Fukushima earthquake (e.g., Asano et al., 2011; Hasegawa et al., 2012) and the onshore seismic network could not detect micro-seismicity around this offshore region. On the other hand, the use of the S-net OBPBs could well constrain the fault modeling of the 2016 off-Fukushima earthquake, which provides an important implication for the crustal stress regime prior to the Tohoku earthquake, even though the S-net was not installed at that time. Such information about the stress regime is important to understand the spatio-temporal change of the intraplate stress state and the generation mechanisms of the intraplate earthquake, especially after a large megathrust earthquake. Our analysis demonstrated that the analysis of the offshore S-net data provided implications for the crustal stress regime at the offshore region, which was difficult to discuss before the S-net was available. Although the S-net OBPB data contains the tsunami-irrelevant pressure change signals, careful analysis of this data significantly improves the constraint of the fault model and will deepen our understanding of the earthquake generation.

7 Conclusions

We examined the S-net tsunami data associated with the off-Fukushima earthquake on 21 November 2016 (M_w 7.1). We first processed the S-net OBPB data and found some pressure signals irrelevant to tsunami were observed: (1) an extremely large drift component and (2) an abrupt pressure step around the origin time. We discussed the cause of these tsunami-irrelevant signals and concluded that these signals were not due to the pressure sensors themselves but probably due to the observation system. We then analyzed the S-net data in order to estimate the tsunami source model and the fault model. Careful analysis of the S-net OBPB data provided the tsunami source distribution, which had a large subsidence with strike angle consistent with the

GCMT solution. Our fault model suggested that the energy-based stress drop of the off-Fukushima earthquake is $\Delta\sigma_E \sim 10$ MPa. The quantitative comparison between the stress drop and the static stress changes caused by the 2011 Tohoku earthquake and its postseismic slip suggested that the additional source of the horizontal extensional stress is necessary to explain the stress drop. We interpreted the stress regime around the off-Fukushima earthquake to be the horizontal extensional even before the Tohoku earthquake, related to the bending of the overriding plate. The S-net pressure data is very useful to constrain the tsunami source model and the finite fault model, even if the model is perturbed by the tsunami-irrelevant signals, which provided an important implication for the tectonic stress regime within the overriding plate.

Data Availability Statement

The S-net OBPB data are available from the website of the National Research Institute for Earth Science and Disaster Resilience [NIED] (NIED, 2019, <https://doi.org/10.17598/NIED.0007>). The NOWPHAS tsunami data is provided upon request to the Port and Airport Research Institute (PARI). The data of the OBPBs installed by ERI was provided upon request to ERI, the University of Tokyo. The OBPB data of Tohoku University was provided upon request to Ryota Hino of Tohoku University. Station locations of the S-net OBPB are available at https://www.seafloor.bosai.go.jp/st_info/. The location of the OBPBs installed by the ERI is available in Gusman et al. (2017). The locations of the NOWPHAS GPS buoys and wave gauges are available at <https://nowphas.mlit.go.jp/pastdata/>. The locations of the OBPBs installed by Tohoku University are listed in Table S2.

We purchased the JTOPO30v2 bathymetry data from the Marine Information Research Center (<http://www.mirc.jha.jp/en/>) of the Japan Hydrographic Association. The plate boundary model in Figure 1 (Nakajima & Hasegawa, 2006) is available from the website of Fuyuki Hirose (<https://www.mri-jma.go.jp/Dep/sei/fhirose/plate/PlateData.html>, in Japanese, accessed on 1 April, 2021). The rotation data of the S-net sensor (Takagi et al., 2019) was provided by Ryota Takagi. The slip models of the mainshock and postseismic slip of Iinuma et al. (2012; 2016) and Tomita et al. (2020) were provided by Takeshi Iinuma and Fumiaki Tomita. The slip distribution models of Gusman et al. (2017), Adriano et al. (2018), and Nakata et al. (2019) are available in each paper. The location of the seafloor bathymetry survey conducted by the Japan Agency for Marine-Earth Science and Technology [JAMSTEC] (blue triangles in

614 Figure 4a) was taken from <http://www.jamstec.go.jp/ceat/j/topics/20161208.html>,
615 http://www.jamstec.go.jp/j/about/press_release/20170301/ (in Japanese).
616

617 **Acknowledgments**

618 The present study was supported by JSPS KAKENHI Grant Number JP19K14818 and
619 JP19H02409 from the Japan Society for the Promotion of Science. Discussions with Ryota Hino,
620 Naoki Uchida, and Tatsuhiko Saito, about interpreting the S-net pressure signals and the results
621 of the fault modeling, were fruitful. We would also like to thank Ryota Takagi, Takeshi Iinuma,
622 and Fumiaki Tomita for providing their useful data.
623

References

- Abe, K. (1977). Tectonic implications of the large shioya-oki earthquakes of 1938. *Tectonophysics*, 41, 269–289. [https://doi.org/10.1016/0040-1951\(77\)90136-6](https://doi.org/10.1016/0040-1951(77)90136-6)
- Adriano, B., Fujii, Y., & Koshimura, S. (2018). Tsunami source and inundation features around Sendai Coast, Japan, due to the November 22, 2016 Mw 6.9 Fukushima earthquake. *Geoscience Letters*, 5, 2. <https://doi.org/10.1186/s40562-017-0100-9>
- Aoi, S., Suzuki, W., Chikasada, N. Y., Miyoshi, T., Arikawa, T., & Seki, K. (2019). Development and utilization of real-time tsunami inundation forecast system using s-net data. *Journal of Disaster Research*, 14(2), 212–224. <https://doi.org/10.20965/jdr.2019.p0212>
- Aoi, S., Asano, Y., Kunugi, T., Kimura, T., Uehira, K., Takahashi, N., & Ueda, H. (2020). MOWLAS : NIED observation network for earthquake , tsunami and volcano. *Earth, Planets and Space*, 72, 126. <https://doi.org/10.1186/s40623-020-01250-x>
- Asano, Y., Saito, T., Ito, Y., Shiomi, K., Hirose, H., Matsumoto, T., ... Sekiguchi, S. (2011). Spatial distribution and focal mechanisms of aftershocks of the 2011 off the Pacific coast of Tohoku Earthquake. *Earth, Planets and Space*, 63, 669–673. <https://doi.org/10.5047/eps.2011.06.016>
- Baba, T., Hirata, K., Hori, T., & Sakaguchi, H. (2006). Offshore geodetic data conducive to the estimation of the afterslip distribution following the 2003 Tokachi-oki earthquake. *Earth and Planetary Science Letters*, 241, 281–292. <https://doi.org/10.1016/j.epsl.2005.10.019>
- Chadwick, W. W. J., Nooner, S. L., Zumberge, M. A., Embley, R. W., & Fox, C. G. (2006). Vertical deformation monitoring at Axial Seamount since its 1998 eruption using deep-sea pressure sensors. *Journal of Volcanology and Geothermal Research*, 150, 313–327. <https://doi.org/10.1016/j.jvolgeores.2005.07.006>
- Fukahata, Y., & Matsu'ura, M. (2016). Deformation of island-arc lithosphere due to steady plate subduction. *Geophysical Journal International*, 204, 825–840. <https://doi.org/10.1093/gji/ggv482>
- Fukuyama, E., Ishida, M., Dreger, D. S., & Kawai, H. (1998). Automated seismic moment tensor determination by using on-line broadband seismic waveforms. *Zisin* 2, 51, 149–156 (in Japanese with English abstract). https://doi.org/10.4294/zisin1948.51.1_149

- 655 Gusman, A. R., Satake, K., Shinohara, M., Sakai, S., & Tanioka, Y. (2017). Fault slip
656 distribution of the 2016 Fukushima earthquake estimated from tsunami waveforms.
657 *Pure and Applied Geophysics*, 174, 2925–2943. [https://doi.org/10.1007/s00024-017-](https://doi.org/10.1007/s00024-017-1590-2)
658 1590-2
- 659 Hardebeck, J. L., & Okada, T. (2018). Temporal stress changes caused by earthquakes: a review.
660 *Journal of Geophysical Research: Solid Earth*, 123, 1350–1365.
661 <https://doi.org/10.1002/2017JB014617>
- 662 Hasegawa, A., Yoshida, K., Asano, Y., Okada, T., Iinuma, T., & Ito, Y. (2012). Change in stress
663 field after the 2011 great Tohoku-Oki earthquake. *Earth and Planetary Science*
664 *Letters*, 355–356, 231–243. <https://doi.org/10.1016/j.epsl.2012.08.042>
- 665 Hashimoto, C., & Matsu'ura, M. (2006). 3-D simulation of tectonic loading at convergent plate
666 boundary zones: Internal stress fields in northeast Japan. *Pure and Applied*
667 *Geophysics*, 163(9), 1803–1817. <https://doi.org/10.1007/s00024-006-0098-y>
- 668 Hino, R. (2015). An overview of the Mw 9, 11 March 2011, Tohoku earthquake. *Summary of the*
669 *Bulletin of the International Seismological Centre*, 48, 100–132.
670 <https://doi.org/10.5281/zenodo.998789>
- 671 Hino, R.? (2021) Ocean bottom pressure gauge data during the 2016 Fukushima-Oki earthquake
672 installed by Tohoku University [Data set]. Zenodo.
673 <http://doi.org/10.5281/zenodo.xxxxxxx>
- 674 Hino, R., Inazu, D., Ohta, Y., Ito, Y., Suzuki, S., Iinuma, T., ... Kaneda, Y. (2014). Was the
675 2011 Tohoku-Oki earthquake preceded by aseismic preslip? Examination of seafloor
676 vertical deformation data near the epicenter. *Marine Geophysical Research*, 35, 181–
677 190. <https://doi.org/10.1007/s11001-013-9208-2>
- 678 Hua, Y., Zhao, D., Toyokuni, G., & Xu, Y. (2020). Tomography of the source zone of the great
679 2011 Tohoku earthquake. *Nature Communications*, 11, 1163. <https://doi.org/10.1038/s41467-020-14745-8>
- 680
- 681 Iinuma, T., Hino, R., Kido, M., Inazu, D., Osada, Y., Ito, Y., ... Miura, S. (2012). Coseismic slip
682 distribution of the 2011 off the Pacific Coast of Tohoku Earthquake (M9.0) refined
683 by means of seafloor geodetic data. *Journal of Geophysical Research*, 117, B07409.
684 <https://doi.org/10.1029/2012JB009186>

- 685 Iinuma, T., Hino, R., Uchida, N., Nakamura, W., Kido, M., Osada, Y., & Miura, S. (2016).
 686 Seafloor observations indicate spatial separation of coseismic and postseismic slips
 687 in the 2011 Tohoku earthquake. *Nature Communications*, 7, 13506.
 688 <https://doi.org/10.1038/ncomms13506>
- 689 Imanishi, K., Ando, R., & Kuwahara, Y. (2012). Unusual shallow normal-faulting earthquake
 690 sequence in compressional northeast Japan activated after the 2011 off the Pacific
 691 coast of Tohoku earthquake. *Geophysical Research Letters*, 39(9), L09306.
 692 <https://doi.org/10.1029/2012GL051491>
- 693 Inazu, D., & Hino, R. (2011). Temperature correction and usefulness of ocean bottom pressure
 694 data from cabled seafloor observatories around Japan for analyses of tsunamis, ocean
 695 tides, and low-frequency geophysical phenomena. *Earth, Planets and Space*, 63(11),
 696 1133–1149. <https://doi.org/10.5047/eps.2011.07.014>
- 697 Inoue, M., Tanioka, Y., & Yamanaka, Y. (2019). Method for near-real time estimation of
 698 Tsunami sources using ocean bottom pressure sensor network (S-net). *Geosciences*,
 699 9, 310. <https://doi.org/10.3390/geosciences9070310>
- 700 Iwata, T., Hirai, A., Inaba, T., & Hirano, M. (2002). Petroleum system in the Offshore Joban
 701 Basin, northeast Japan. *Journal of the Japanese Association for Petroleum*
 702 *Technology*, 67(1), 62–71 (in Japanese with English abstract).
 703 https://doi.org/10.3720/japt.67.1_62
- 704 Kanamori, H., & Anderson, D. L. (1975). Theoretical basis of some empirical relations in
 705 seismology. *Bulletin of the Seismological Society of America*, 65(5), 1073–1095.
- 706 Kanazawa, T., & Hasegawa, A. (1997). Ocean-bottom observatory for earthquakes and tsunami
 707 off Sanriku, north-eastern Japan using submarine cable. *Proceedings of International*
 708 *Workshop on Scientific Use of Submarine Cables*, 208–209.
- 709 Kanazawa, T., Uehira, K., Mochizuki, M., Shinbo, T., Fujimoto, H., Noguchi, S., et al. (2016).
 710 *S-net project, cabled observation network for earthquake and tsunamis* [Conference
 711 presentation]. Suboptic2016, Dubai.
 712 [https://suboptic.org/wp-content/uploads/fromke-vin/program/WE2B.3%20S-net](https://suboptic.org/wp-content/uploads/fromke-vin/program/WE2B.3%20S-net%20Project,%20Cabled%20Observation%20Network%20for%20Earthquakes%20and%20Tsunamis.pdf)
 713 [%20Project,%20Cabled%20Observation%20Network%20for%20Earthquakes](https://suboptic.org/wp-content/uploads/fromke-vin/program/WE2B.3%20S-net%20Project,%20Cabled%20Observation%20Network%20for%20Earthquakes%20and%20Tsunamis.pdf)
 714 [%20and%20Tsunamis.pdf](https://suboptic.org/wp-content/uploads/fromke-vin/program/WE2B.3%20S-net%20Project,%20Cabled%20Observation%20Network%20for%20Earthquakes%20and%20Tsunamis.pdf)

- Kawaguchi, K., Sakuraba, S., Nagai, T., Nakai, K., Nukada, K., & Murase, H. (2017). Characteristics of observed low frequency wave profiles of the 2016 Fukushima-Off earthquake at offshore, shallow sea and coastal stations. *Journal of Japan Society of Civil Engineers, Ser. B3 (Ocean Engineering)*, 73(2), I_743-I_748. https://doi.org/10.2208/jscejoe.73.I_743
- Kodaira, S., Fujiwara, T., Fujie, G., Nakamura, Y., & Kanamatsu, T. (2020). Large coseismic slip to the trench during the 2011 Tohoku-Oki earthquake. *Annual Review of Earth and Planetary Sciences*, 48, 321–343. <https://doi.org/10.1146/annurev-earth-071719-055216>
- Kodaira, S., Iinuma, T., & Imai, K. (2021). Investigating a tsunamigenic megathrust earthquake in the Japan Trench. *Science*, 371, eabe1169. <https://doi.org/10.1126/science.abe1169>
- Kubota, T., Hino, R., Inazu, D., Ito, Y., & Iinuma, T. (2015). Complicated rupture process of the Mw 7.0 intraslab strike-slip earthquake in the Tohoku region on 10 July 2011 revealed by near-field pressure records. *Geophysical Research Letters*, 42, 9733–9739. <https://doi.org/10.1002/2015GL066101>
- Kubota, T., Suzuki, W., Nakamura, T., Chikasada, N. Y., Aoi, S., Takahashi, N., & Hino, R. (2018). Tsunami source inversion using time-derivative waveform of offshore pressure records to reduce effects of non-tsunami components. *Geophysical Journal International*, 215, 1200–1214. <https://doi.org/10.1093/gji/ggy345>
- Kubota, T., Saito, T., Ito, Y., Kaneko, Y., Wallace, L. M., Suzuki, S., Hino, R., & Henrys, S. (2018). Using tsunami waves reflected at the coast to improve offshore earthquake source parameters: application to the 2016 Mw 7.1 Te Araroa earthquake, New Zealand. *Journal of Geophysical Research: Solid Earth*, 123, 8767–8779. <https://doi.org/10.1029/2018JB015832>
- Kubota, T., Saito, T., & Suzuki, W. (2020). Millimeter-scale tsunami detected by a wide and dense observation array in the deep ocean: Fault modeling of an Mw 6.0 interplate earthquake off Sanriku, NE Japan. *Geophysical Research Letters*, 47, e2019GL085842. <https://doi.org/10.1029/2019GL085842>
- Kubota, T., Saito, T., Chikasada, N. Y., & Suzuki, W. (2020). Ultrabroadband seismic and tsunami wave observation of high-sampling ocean-bottom pressure gauge covering

- 745 periods from seconds to hours. *Earth and Space Science*, 7, e2020EA001197. <https://doi.org/10.1029/2020ea001197>
- 746
- 747 Kubota, T., Saito, T., Chikasada, N. Y., & Sandanbata, O. (2021). Meteotsunami observed by the
- 748 deep-ocean seafloor pressure gauge network off northeastern Japan. [Preprint]. *Earth*
- 749 *and Space Science Open Archive*. <https://doi.org/10.1002/essoar.10506159.1>
- 750 Lay, T. (2018). A review of the rupture characteristics of the 2011 Tohoku-oki Mw 9.1
- 751 earthquake. *Tectonophysics*, 733, 4–36. <https://doi.org/10.1016/j.tecto.2017.09.022>
- 752 Matsubara, M., Sato, H., Uehira, K., Mochizuki, M., Kanazawa, T., Takahashi, N., Suzuki, K., &
- 753 Kamiya, S. (2019). Seismic velocity structure in and around the Japanese Island src
- 754 derived from seismic tomography including NIED MOWLAS Hi-net and S-net data.
- 755 In M. Kanao & G. Toyokuni (Eds.), *Seismic Waves - Probing Earth System*.
- 756 IntechOpen. <https://doi.org/10.5772/intechopen.86936>.
- 757 Matsumoto, K., Takanezawa, T., & Ooe, M. (2000). Ocean tide models developed by
- 758 assimilating TOPEX/POSEIDON altimeter data into hydrodynamical model: A
- 759 global model and a regional model around Japan. *Journal of Oceanography*, 56,
- 760 567–581. <https://doi.org/10.1023/A:1011157212596>
- 761 Miyakoshi, K., Somei, K., Yoshida, K., Kurahashi, S., Irikura, K., & Kamae, K. (2020). Scaling
- 762 Relationships of Source Parameters of Inland Crustal Earthquakes in Tectonically
- 763 Active Regions. *Pure and Applied Geophysics*, 177, 1917–1929.
- 764 <https://doi.org/10.1007/s00024-019-02160-0>
- 765 Mochizuki, M., Kanazawa, T., Uehira, K., Shimbo, T., Shiomi, K., Kunugi, T., et al. (2016). S-
- 766 net project: Construction of large scale seafloor observatory network for tsunamis
- 767 and earthquakes in Japan [Conference presentation]. AGU Fall Meeting 2016,
- 768 American Geophysical Union, San Francisco.
- 769 Mulia, I. E., & Satake, K. (2021). Synthetic analysis of the efficacy of the S-net system in
- 770 tsunami forecasting. *Earth, Planets and Space*, 73, 36.
- 771 <https://doi.org/10.1186/s40623-021-01368-6>
- 772 Murotani, S., Satake, K., & Fujii, Y. (2013). Scaling relations of seismic moment, rupture area,
- 773 average slip, and asperity size for M~9 subduction-zone earthquakes. *Geophysical*
- 774 *Research Letters*, 40, 5070–5074. <https://doi.org/10.1002/grl.50976>

- 775 Murotani, S. (2018) Natural disasters that reached a milestone in Fukushima –The 1888 eruption
776 of Bandai-san and the 1938 Fukushima-ken Toho-oki Earthquake– [Translated Title
777 from Japanese]. *Earthquake Journal*, 66, 30–39 (in Japanese). Retrieved January 16,
778 2021, from <https://www.adeq.or.jp/public/img/66.pdf>
- 779 Nagai, T. (1998). Development and improvement of the Japanese coastal wave observation
780 network (NOWPHAS). *Journal of Japan Society of Civil Engineers*, 609, 1–14.
781 https://doi.org/10.2208/jscej.1998.609_1
- 782 Nakajima, J., & Hasegawa, A. (2006). Anomalous low-velocity zone and linear alignment of
783 seismicity along it in the subducted Pacific slab beneath Kanto, Japan: Reactivation
784 of subducted fracture zone? *Geophysical Research Letters*, 33, L16309.
785 <https://doi.org/10.1029/2006GL026773>
- 786 Nakata, K., Hayashi, Y., Tsushima, H., Fujita, K., Yoshida, Y., & Katsumata, A. (2019).
787 Performance of uniform and heterogeneous slip distributions for the modeling of the
788 November 2016 off Fukushima earthquake and tsunami, Japan. *Earth, Planets and*
789 *Space*, 71(1), 30. <https://doi.org/10.1186/s40623-019-1010-1>
- 790 National Research Institute for Earth Science and Disaster Resilience [NIED] (2019). NIED S-
791 net [Data set]. <https://doi.org/10.17598/nied.0007>
- 792 Nishikawa, T., Matsuzawa, T., Ohta, K., Uchida, N., Nishimura, T., & Ide, S. (2019). The slow
793 earthquake spectrum in the Japan Trench illuminated by the S-net seafloor
794 observatories. *Science*, 365, 808–813. <https://doi.org/10.1126/science.aax5618>
- 795 Noda, H., Lapusta, N., & Kanamori, H. (2013). Comparison of average stress drop measures for
796 ruptures with heterogeneous stress change and implications for earthquake physics.
797 *Geophysical Journal International*, 193, 1691–1712.
798 <https://doi.org/10.1093/gji/ggt074>
- 799 Polster, A., Fabian, M., & Villinger, H. (2009). Effective resolution and drift of parascientific
800 pressure sensors derived from long-term seafloor measurements. *Geochemistry,*
801 *Geophysics, Geosystems*, 10(8), Q08008. <https://doi.org/10.1029/2009GC002532>
- 802 Saito, T. (2019). *Tsunami generation and propagation*. Springer Japan, Tokyo.
803 <https://doi.org/10.1007/978-4-431-56850-6>

- 804 Saito, T., Satake, K., & Furumura, T. (2010). Tsunami waveform inversion including dispersive
805 waves: The 2004 earthquake off Kii Peninsula, Japan. *Journal of Geophysical*
806 *Research*, 115, B06303. <https://doi.org/10.1029/2009JB006884>
- 807 Saito, T., & Kubota, T. (2020). Tsunami modeling for the deep sea and inside focal areas.
808 *Annual Review of Earth and Planetary Sciences*, 48, 121–145.
809 <https://doi.org/10.1146/annurev-earth-071719-054845>
- 810 Saito, T., Kubota, T., Chikasada, N. Y., Tanaka, Y., & Sandanbata, O. (2021). Meteorological
811 tsunami generation due to sea-surface pressure change: Three-dimensional theory
812 and synthetics of ocean-bottom pressure change [Preprint]. *Earth and Space Science*
813 *Open Archive*. <https://doi.org/10.1002/essoar.10504961.1>
- 814 Sawazaki, K., & Nakamura, T. (2020). “N”-shaped Y/X coda spectral ratio observed for in-line-
815 type OBS networks; S-net and ETMC: interpretation based on natural vibration of
816 pressure vessel. *Earth, Planets and Space*, 72, 130. [https://doi.org/10.1186/s40623-](https://doi.org/10.1186/s40623-020-01255-6)
817 [020-01255-6](https://doi.org/10.1186/s40623-020-01255-6)
- 818 Somerville, P., Irikura, K., Graves, R., Sawada, S., Wald, D., Abrahamson, N., Iwasaki, Y.,
819 Kagawa, T., Smith, N., & Kowada, A. (1999). Characterizing crustal earthquake slip
820 models for the prediction of strong ground motion. *Seismological Research Letters*,
821 70, 59–80. <https://doi.org/10.1785/gssrl.70.1.59>
- 822 Sun, T., Wang, K., Iinuma, T., Hino, R., He, J., Fujimoto, H., ... Hu, Y. (2014). Prevalence of
823 viscoelastic relaxation after the 2011 Tohoku-oki earthquake. *Nature*, 514(7520), 84–
824 87. <https://doi.org/10.1038/nature13778>
- 825 Suppasri, A., Leelawat, N., Latcharote, P., Roeber, V., Yamashita, K., Hayashi, A., ... Imamura,
826 F. (2017). The 2016 Fukushima earthquake and tsunami: Local tsunami behavior and
827 recommendations for tsunami disaster risk reduction. *International Journal of*
828 *Disaster Risk Reduction*, 21, 323–330. <https://doi.org/10.1016/j.ijdr.2016.12.016>
- 829 Takagi, R., Uchida, N., Nakayama, T., Azuma, R., Ishigami, A., Okada, T., ... Shiomi, K.
830 (2019). Estimation of the orientations of the S-net cabled ocean-bottom sensors.
831 *Seismological Research Letters*, 90, 2175–2187. <https://doi.org/10.1785/0220190093>
- 832 Takagi, R., Toyokuni, G., & Chikasada, N. (2020). Ambient noise correlation analysis of S-net
833 records: extracting surface wave signals below instrument noise levels. *Geophysical*
834 *Journal International*, 224, 1640–1657. <https://doi.org/10.1093/gji/ggaa548>

- 835 Tanaka, M., Asano, K., Iwata, T., & Kubo, H. (2014). Source rupture process of the 2011
836 Fukushima-ken Hamadori earthquake: How did the two subparallel faults rupture?
837 *Earth, Planets and Space*, 66(1), 101. <https://doi.org/10.1186/1880-5981-66-101>
- 838 Tanaka, S., Matsuzawa, T., & Asano, Y. (2019). Shallow Low-Frequency Tremor in the
839 Northern Japan Trench Subduction Zone. *Geophysical Research Letters*, 46, 5217–
840 5224. <https://doi.org/10.1029/2019GL082817>
- 841 Tanioka, Y. (2020). Improvement of Near-field Tsunami Forecasting Method Using Ocean
842 Bottom Pressure Sensor Network (S-net). *Earth, Planets and Space*, 72, 132. <https://doi.org/10.1186/s40623-020-01268-1>
- 843
- 844 Terakawa, T., & Matsu'ura, M. (2010). The 3-D tectonic stress fields in and around Japan
845 inverted from centroid moment tensor data of seismic events. *Tectonics*, 29, TC6008.
846 <https://doi.org/10.1029/2009TC002626>
- 847 Toda, S., & Goto, H. (2016)
848 [https://irides.tohoku.ac.jp/media/files/earthquake/eq/2016_fukushima_eq/](https://irides.tohoku.ac.jp/media/files/earthquake/eq/2016_fukushima_eq/20161122_fukushima_eq_activefault_toda.pdf)
849 [20161122_fukushima_eq_activefault_toda.pdf](https://irides.tohoku.ac.jp/media/files/earthquake/eq/2016_fukushima_eq/20161122_fukushima_eq_activefault_toda.pdf)
- 850 Tomita, F., Kido, M., Osada, Y., Hino, R., Ohta, Y., & Iinuma, T. (2015). First measurement of
851 the displacement rate of the Pacific Plate near the Japan Trench after the 2011
852 Tohoku-Oki earthquake using GPS/acoustic technique. *Geophysical Research*
853 *Letters*, 42(20), 8391–8397. <https://doi.org/10.1002/2015GL065746>
- 854 Tomita, F., Kido, M., Ohta, Y., Iinuma, T., & Hino, R. (2017). Along-trench variation in seafloor
855 displacements after the 2011 Tohoku earthquake. *Science Advances*, 3, e1700113.
856 <https://doi.org/10.1126/sciadv.1700113>
- 857 Tomita, F., Iinuma, T., Ohta, Y., Hino, R., Kido, M., & Uchida, N. (2020). Improvement on
858 spatial resolution of a coseismic slip distribution using postseismic geodetic data
859 through a viscoelastic inversion. *Earth, Planets and Space*, 72, 84.
860 <https://doi.org/10.1186/s40623-020-01207-0>
- 861 Tsushima, H., Hino, R., Tanioka, Y., Imamura, F., & Fujimoto, H. (2012). Tsunami waveform
862 inversion incorporating permanent seafloor deformation and its application to
863 tsunami forecasting. *Journal of Geophysical Research*, 117, B03311. <https://doi.org/10.1029/2011JB008877>
- 864

- 865 Tsushima, H., & Yamamoto, T. (2020). *Operational use of tsunami source inversion in near-*
866 *field tsunami warning by JMA* [Conference presentation]. JpGU-AGU Joint Meeting
867 2020 Virtual, Online. [https://confit.atlas.jp/guide/event/jpgu2020/subject/HDS08-12/](https://confit.atlas.jp/guide/event/jpgu2020/subject/HDS08-12/advanced)
868 advanced
- 869 Uchida, N., Nakajima, J., Wang, K., Takagi, R., Yoshida, K., Nakayama, T., ... Asano, Y.
870 (2020). Stagnant forearc mantle wedge inferred from mapping of shear-wave
871 anisotropy using S-net seafloor seismometers. *Nature Communications*, 11.
872 <https://doi.org/10.1038/s41467-020-19541-y>
- 873 Uchida, N. & Burgmann, R. (2021). A Decade of Lessons Learned from the 2011 Tohoku-oki
874 Earthquake [Preprint]. *Earth and Space Open Archive*.
875 <https://doi.org/10.1002/essoar.10505694.1>
- 876 Uehira, K., Kanazawa, T., Mochizuki, M., Fujimoto, H., Noguchi, S., Shinbo, T., et al. (2016).
877 *Outline of seafloor observation network for earthquakes and tsunamis along the*
878 *Japan Trench (S-net)* [Conference presentation]. EGU General Assembly 2016,
879 European Geosciences Union, Vienna, Austria.
- 880 Wallace, L. M., Araki, E., Saffer, D., Wang, X., Roesner, A., Kopf, A., ... Carr, S. (2016). Near-
881 field observations of an offshore Mw 6.0 earthquake from an integrated seafloor and
882 subseafloor monitoring network at the Nankai Trough, southwest Japan. *Journal of*
883 *Geophysical Research: Solid Earth*, 121, 8338–8351.
884 <https://doi.org/10.1002/2016JB013417>
- 885 Wells, D. L., & Coppersmith, K. J. (1994). New empirical relationships among magnitude,
886 rupture length, rupture width, rupture area, and surface displacement. *Bulletin of the*
887 *Seismological Society of America*, 84(4), 974–1002.
- 888 Wang, K., & Suyehiro, K. (1999). How does plate coupling affect crustal stresses in Northeast
889 and Southwest Japan? *Geophysical Research Letters*, 26(15), 2307–2310.
890 <https://doi.org/10.1029/1999GL900528>
- 891 Wang, K., Sun, T., Brown, L., Hino, R., Tomita, F., Kido, M., ... Fujiwara, T. (2018). Learning
892 from crustal deformation associated with the M9 2011 Tohoku-oki earthquake.
893 *Geosphere*, 14, 1–20. <https://doi.org/10.1130/GES01531.1>
- 894 Wang, K., Brown, L., Hu, Y., Yoshida, K., He, J., & Sun, T. (2019). Stable Forearc Stressed by a
895 Weak Megathrust: Mechanical and Geodynamic Implications of Stress Changes

- Caused by the M = 9 Tohoku-Oki Earthquake. *Journal of Geophysical Research: Solid Earth*, 124, 6179–6194. <https://doi.org/10.1029/2018JB017043>
- Wang, Y., & Satake, K. (2021). Real-time tsunami data assimilation of S-net pressure gauge records during the 2016 Fukushima Earthquake. *Seismological Research Letters*. <https://doi.org/10.1785/0220200447>
- Watts, D. R., & Kontoyiannis, H. (1990). Deep-ocean bottom pressure measurement: drift removal and performance. *Journal of Atmospheric and Oceanic Technology*, 7, 296–306. [https://doi.org/10.1175/1520-0426\(1990\)007<0296:DOBPMD>2.0.CO;2](https://doi.org/10.1175/1520-0426(1990)007<0296:DOBPMD>2.0.CO;2)
- Yamamoto, N., Aoi, S., Hirata, K., Suzuki, W., Kunugi, T., & Nakamura, H. (2016). Multi-index method using offshore ocean-bottom pressure data for real-time tsunami forecast. *Earth, Planets and Space*, 68, 128. <https://doi.org/10.1186/s40623-016-0500-7>
- Yamamoto, N., Hirata, K., Aoi, S., Suzuki, W., Nakamura, H., & Kunugi, T. (2016). Rapid estimation of tsunami source centroid location using a dense offshore observation network. *Geophysical Research Letters*, 43, 4263–4269. <https://doi.org/10.1002/2016GL068169>
- Yoshida, K., Hasegawa, A., Okada, T., Iinuma, T., Ito, Y., & Asano, Y. (2012). Stress before and after the 2011 great Tohoku-oki earthquake and induced earthquakes in inland areas of eastern Japan. *Geophysical Research Letters*, 39(3), L03302. <https://doi.org/10.1029/2011GL049729>
- Yoshida, K., Hasegawa, A., & Okada, T. (2015a). Spatial variation of stress orientations in NE Japan revealed by dense seismic observations. *Tectonophysics*, 647, 63–72. <https://doi.org/10.1016/j.tecto.2015.02.013>
- Yoshida, K., Hasegawa, A., & Okada, T. (2015b). Spatially heterogeneous stress field in the source area of the 2011 Mw 6.6 Fukushima-Hamadori earthquake, NE Japan, probably caused by static stress change. *Geophysical Journal International*, 201, 1062–1071. <https://doi.org/10.1093/gji/ggv068>
- Yu, Z., & Zhao, D. (2020). Seismic evidence for water transportation in the forearc off northern Japan. *Journal of Geophysical Research: Solid Earth*, 125, 2019JB018600. <https://doi.org/10.1029/2019jb018600>

927

928 **Table 1.** Fault parameters for the rectangular fault models.

Models	Fault center location			M_0 [Nm]	Maximum vertical displacement [cm]	
	Longitude [°E]	Latitude [°N]	Depth [km] ^a		Uplift	Subsidence
GCMT solution	141.46	37.31	12.0	3.18×10^{19}	N/A	N/A
Tsunami source	N/A	N/A	N/A	N/A	16.3	238.4
Grid-search ^{ab}	141.5165	37.3105	6.0	2.10×10^{19}	16.0	193.1
Slip distribution ^a	141.4908 ^c	37.2630 ^c	7.7 ^c	6.30×10^{19}	10.5	237.4
Gusman et al. (2017)	N/A	N/A	N/A	3.70×10^{19}	10.1	182.6
Adriano et al. (2018)	N/A	N/A	N/A	3.35×10^{19}	8.5	130.6
Nakata et al. (2019)	N/A	N/A	N/A	8.52×10^{19}	29.7	222.2

929 ^aFault geometry is fixed to the GCMT value; strike = 49°, dip = 35°, rake = −89°.930 ^bFault dimension is $L = 15$ km, $W = 10$ km, and slip amount is $D = 467.7$ cm. The depths of the fault top and bottom are 3.1 km and 8.9
931 km, respectively.932 ^cSlip-weighted average location is shown.

933

934

Improving the constraint on the M_w 7.1 2016 off-Fukushima shallow normal-faulting earthquake with the high azimuthal coverage tsunami data from the S-net wide and dense network: Implication for the stress regime in the Tohoku overriding plate

T. Kubota¹, H. Kubo¹, K. Yoshida², N. Y. Chikasada¹, W. Suzuki¹,
T. Nakamura³, and H. Tsushima⁴

¹ National Research Institute for Earth Science and Disaster Resilience, Japan.

² Graduate School of Science, Tohoku University, Japan.

³ Central Research Institute of Electric Power Industry, Japan.

Contents of this file

Text S1
Figures S1 to S5
Tables S1 to S2

Introduction

Text S1 explains the procedure for the inversion analysis. Figure S1 shows the trade-off curve used to determine the weight of the smoothing constraint. Figure S2 is the result of the tsunami source inversion using the pressure waveforms. Figure S3 is the result of the grid-search analysis. The forward simulation of the tsunami waveforms based on the finite fault model is shown in Figures S4 and S5. Table S1 shows the unknown parameters searched in the grid-search analysis. The station locations of the OBPBs installed by Tohoku University are listed in Table S2.

Text S1

This text explains the procedure for the tsunami source modeling shown in Section 4. We first explain how to simulate the tsunami Green's function, which are the pressure change waveforms due to the tsunami and seafloor displacement at each OBPB caused by the displacement of the small region of seafloor. We distribute the small elements of the seafloor uplift (unit source elements) around the focal area (rectangular area in Figure 4a). The unit source element of the seafloor vertical displacement is given by

$$u_{ij}(x, y) = u_0 \left[\frac{1}{2} + \frac{1}{2} \cos \left(\frac{2\pi(x-x_i)}{L_x} \right) \right] \left[\frac{1}{2} + \frac{1}{2} \cos \left(\frac{2\pi(y-y_j)}{L_y} \right) \right] \\ \text{for } x_i - \frac{L_x}{2} \leq x \leq x_i + \frac{L_x}{2}, y_j - \frac{L_y}{2} \leq y \leq y_j + \frac{L_y}{2}, \quad (\text{S1})$$

which takes the maximum value of $u_0 = 1$ cm at (x_i, y_j) . Here, L_x and L_y are the spatial extent of the unit source element along the x - and y -directions, respectively. We assume that $L_x = L_y = 4$ km. Each of the unit sources overlaps with adjacent unit sources with a horizontal interval of $\Delta L_x = L_x/2$ and $\Delta L_y = L_y/2$. The numbers of unit sources along the x -direction and y -directions are $N_x = 25$ and $N_y = 25$, respectively, and the total number of unit sources is $N = N_x \times N_y = 625$. The size of the analytical area where the unit sources are distributed is 50 km \times 50 km.

Using the seafloor vertical displacement from the unit sources, we calculate tsunamis using the following procedure. We assume the initial sea-surface height change assuming that the sea-surface displacement is equal to the seafloor displacement. We then solve the linear dispersive tsunami equation (Saito et al., 2010; Saito, 2019) in Cartesian coordinates with the staggered grid in order to simulate tsunamis:

$$\begin{aligned} \frac{\partial M}{\partial t} + gh \frac{\partial \eta}{\partial x} &= \frac{1}{3} h^2 \frac{\partial^2}{\partial x \partial t} \left(\frac{\partial M}{\partial x} + \frac{\partial N}{\partial y} \right) \\ \frac{\partial N}{\partial t} + gh \frac{\partial \eta}{\partial y} &= \frac{1}{3} h^2 \frac{\partial^2}{\partial y \partial t} \left(\frac{\partial M}{\partial x} + \frac{\partial N}{\partial y} \right), \\ \frac{\partial \eta}{\partial t} &= -\frac{\partial M}{\partial x} - \frac{\partial N}{\partial y} \end{aligned} \quad (\text{S2})$$

where the variable η is the sea surface height anomaly (tsunami height), M and N are the velocity components integrated along the vertical direction over the seawater depth, h is the water depth, and g is the gravitational constant. For water depth h , we use the JTOPO30 data with a spatial resolution of 30 arcsec, provided by the Marine Information Research Center of the Japan Hydrographic Association (<http://www.mirc.jha.jp/en/>), interpolating the spatial interval of $\Delta x = \Delta y = 1$ km. We assume that the displacement occurs instantaneously, at time $t = 0$ s. The temporal interval of the calculation is $\Delta t = 1$ s. After the calculation, we subtract the pressure offset change due to the seafloor displacement (Tsushima et al., 2012), assuming that a seawater column height change of 1 cm H₂O is equal to a pressure change of 1 hPa. We finally apply the same bandpass filter to the simulated waveform as that applied to the observation.

In order to estimate the tsunami source, we use the time-derivative waveforms of the bandpass-filtered pressure waveforms for the inversion analysis ($\partial p / \partial t$, Figure 4c), because the time-derivative of the step signal becomes the impulse signal and thus does not contain the offset change, which can reduce the artificials due to the tsunami-irrelevant steps (Kubota, Suzuki et al., 2018). The data time window used for the modeling, which includes the main part of the tsunami (indicated by the blue traces in Figure 4c), is manually determined. We solve the following observation equation:

$$\begin{pmatrix} \mathbf{d} \\ \mathbf{0} \end{pmatrix} = \begin{pmatrix} \mathbf{H} \\ \alpha \mathbf{S} \end{pmatrix} \mathbf{m} \quad (\text{S3})$$

The data vector \mathbf{d} consists of the time-derivative waveforms of the observed pressure $\partial p / \partial t$, and the matrix \mathbf{H} consists of the time-derivative of the tsunami Green's functions. The vector \mathbf{m} consists of the amounts of the displacement of the unit sources, which are the unknown parameters to be solved. The matrix \mathbf{S} indicates the constraint for the spatial smoothing (e.g., Baba et al., 2006) and the parameter α is its weight. The goodness of the estimated source is evaluated using the variance reduction (VR):

$$\text{VR} = \left(1 - \frac{\sum_i (d_i^{\text{obs}} - d_i^{\text{cal}})^2}{\sum_i d_i^{\text{obs}^2}} \right) \times 100 (\%) \quad (\text{S4})$$

where d_i^{obs} and d_i^{cal} are the i -th data of the observed and calculated time-derivative pressure waveforms, respectively. The smoothing weight α is determined based on the trade-off between the weight and the VR (Figure S1) in order to avoid both the overfitting and oversmoothing of data.

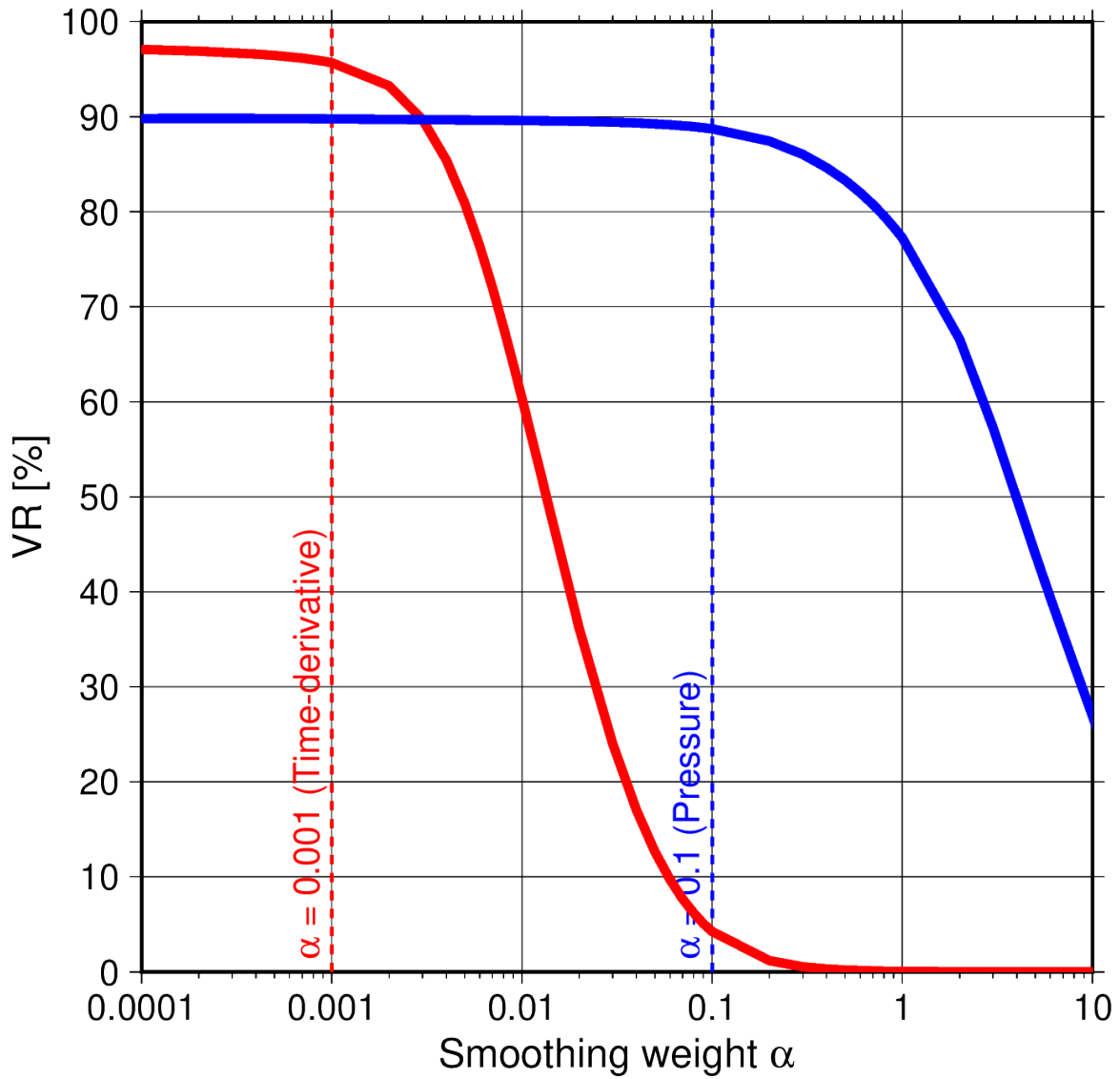


Figure S1. Trade-off curve between the smoothing weight α and VR. Red and blue solid lines are the trade-off curves for the inversions using the time-derivative waveform of the pressure (Figure 4) and the pressure waveform (Figure S2), respectively. Dashed lines denote the weight values used for the inversion analyses.

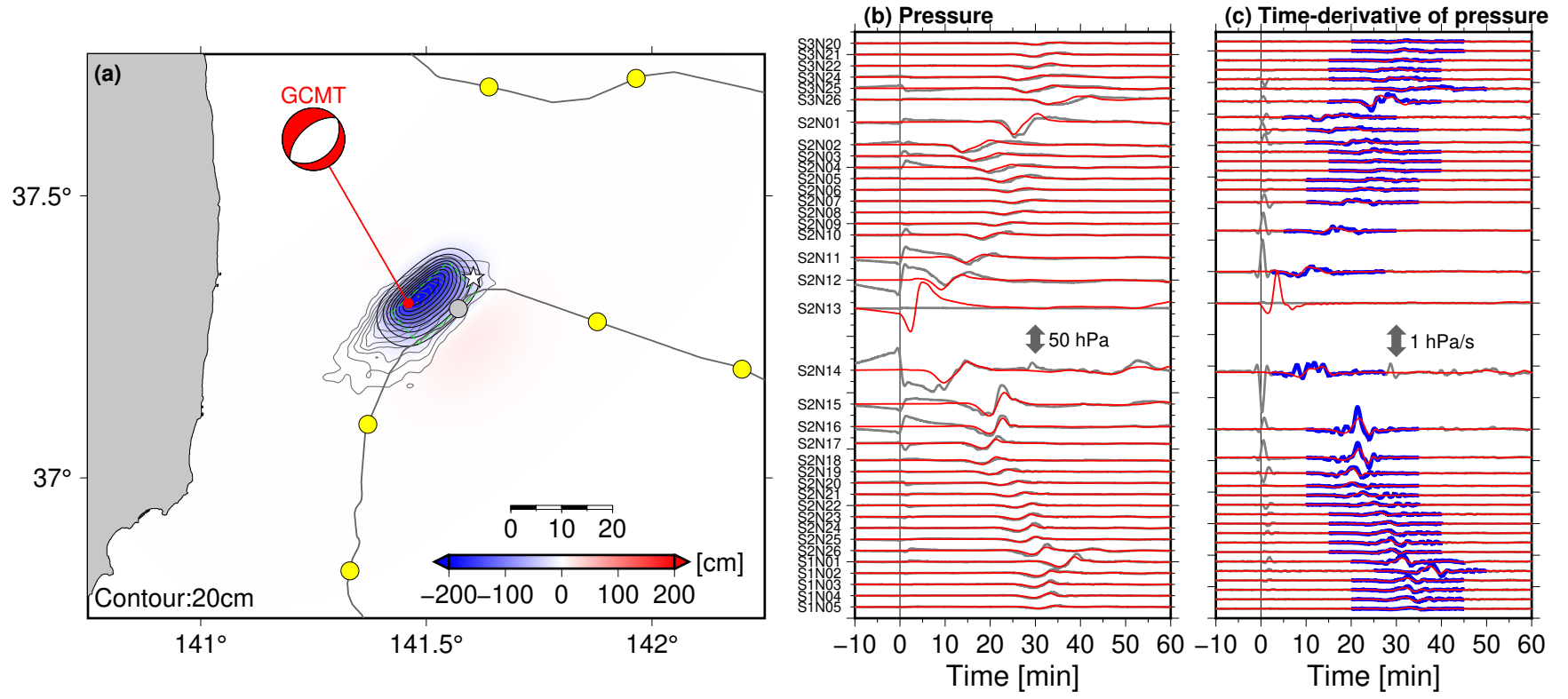


Figure S3. Results of the grid-search analysis. (a) Spatial distribution of the tsunami source. The green rectangle shows the location of the rectangular fault model. Comparisons of (b) the pressure waveforms and (c) the time-derivative waveforms. See Figure 4 for a detailed explanation of the figure.

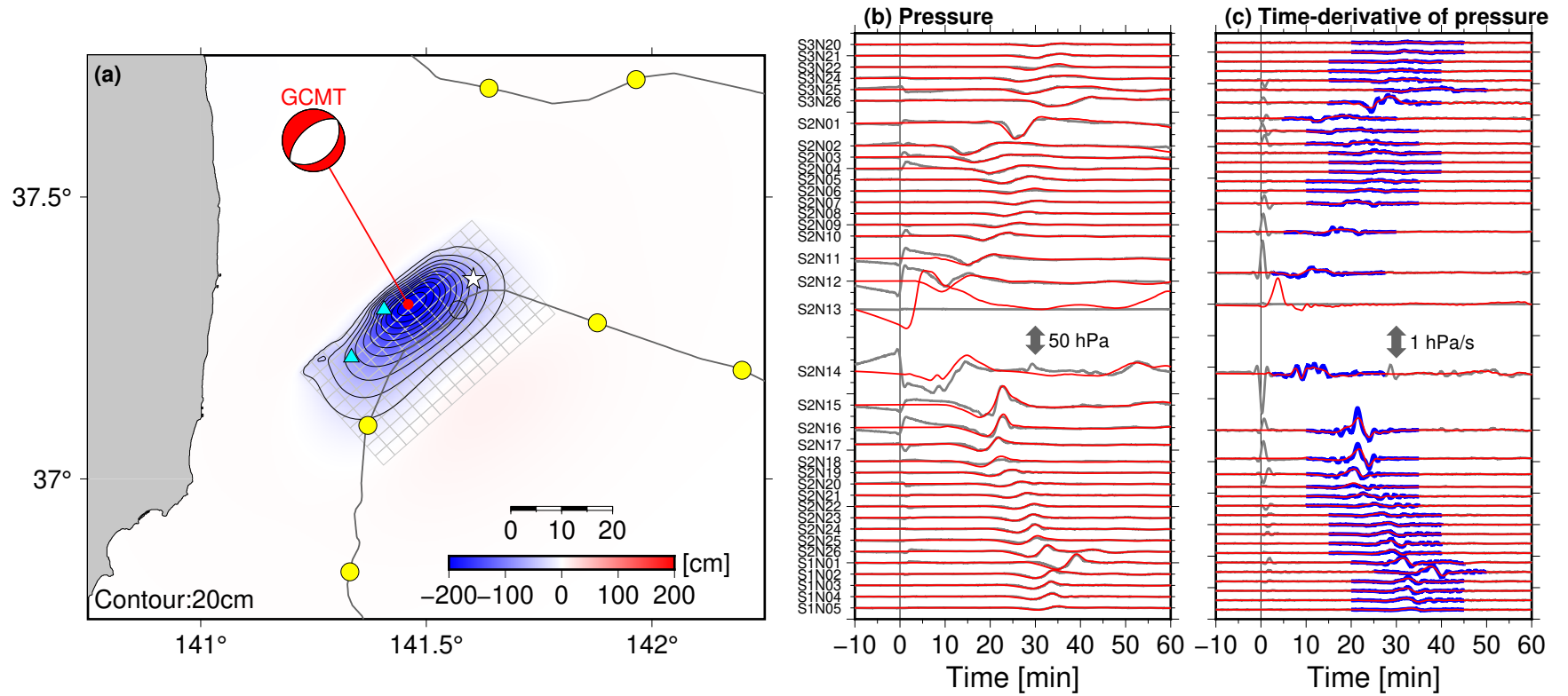


Figure S4. Results of the slip inversion. (a) Spatial distribution of the tsunami source calculated from the slip distribution in Figure 8a. Comparisons of (b) the pressure waveforms and (c) the time-derivative waveforms. See Figure 4 for a detailed explanation of the figure.

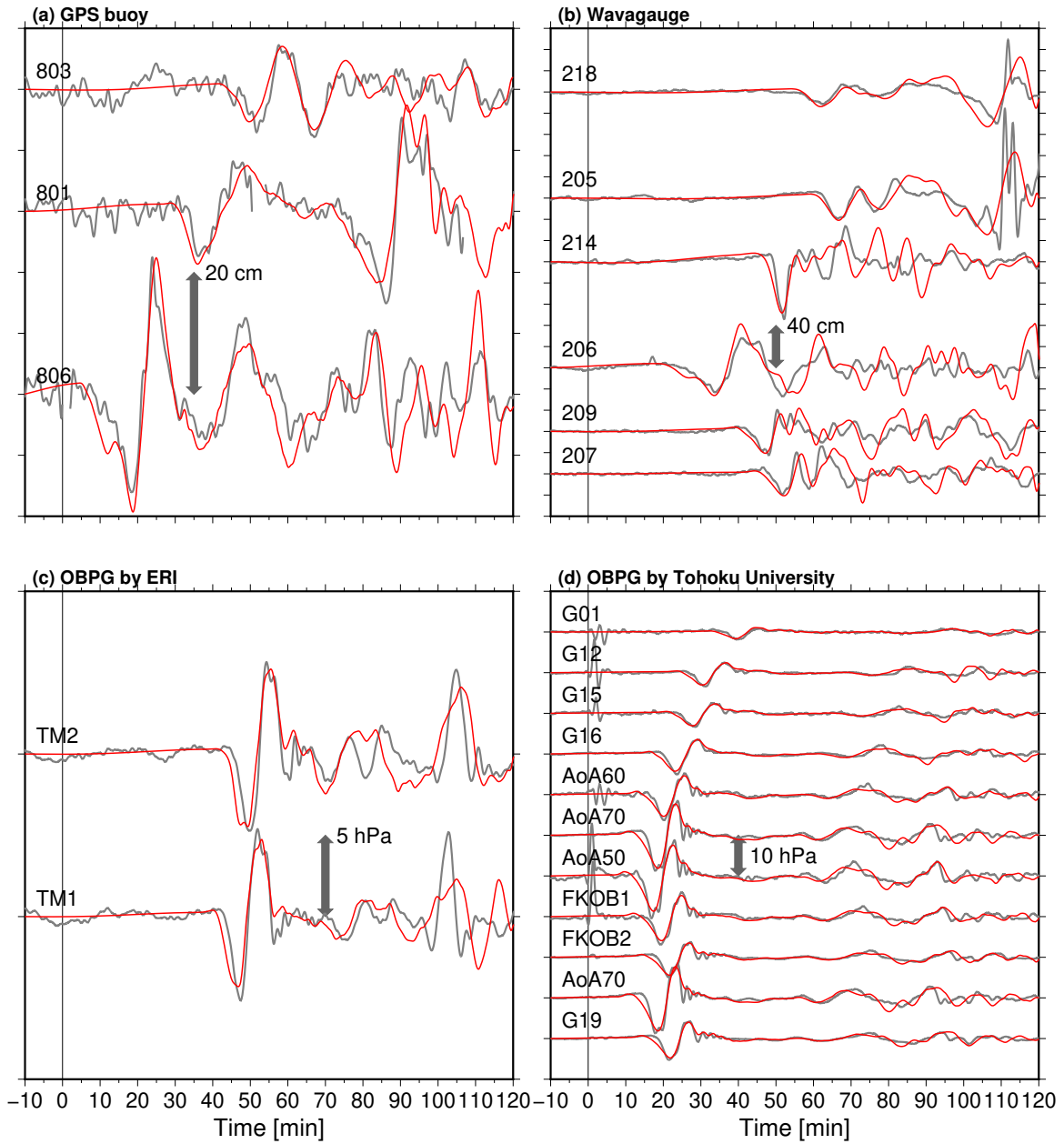


Figure S5. Waveform comparisons for the other tsunami stations from the finite fault model for (a) NOWPHAS Near-coastal GPS buoys, (b) NOWPHAS wave gauges, (c) OBPGs installed by ERI, and (d) OBPGs installed by Tohoku University. See Figure 1 for station locations.

Table S1. Search range for the grid search analysis.

Parameters	Range	Increment
Longitude ^{ab}	141.46°E ± 20 km	5 km
Latitude ^{ab}	37.31°N ± 20 km	5 km
Depth ^{ab}	12.0 km ± 10 km ^a	2 km
Strike ^a	49°	Fixed
Dip ^a	35°	Fixed
Rake ^a	−89°	Fixed
Length ^c	5 km – 60 km	5 km
Width ^c	5 km – 60 km	5 km
Slip amount	Adjusted so that the VR value takes the maximum	

^aReference values are taken from the GCMT solution.

^bFault center location is shown.

^cWhen the depth of the updip end of the fault is shallower than a depth of 0.1 km, the calculation is skipped.

Table S2. Station list of the OBPBs installed by Tohoku University

Station	Longitude (°E)	Latitude (°N)	Depth (m)	Observation duration (yyyy/mm/dd)	Logger type ^a
G01	144.9204	38.7030	5456	2016/05/22 – 2017/04/11	UME
G12	143.5317	38.0213	4366	2016/05/24 – 2017/04/10	UME
G16	143.0470	37.3324	4414	2016/05/27 – 2017/04/15	HAK
G17 ^b	142.7123	36.8979	4232	2016/05/28 – 2017/04/09	HAK
G19	142.6735	36.4931	5691	2016/05/28 – 2017/04/09	HAK
AoA50	142.3176	36.8725	2853	2016/09/22 – 2017/11/09	UME
AoA60 ^b	142.7140	36.8993	4225	2016/09/22 – 2017/10/15	UME
AoA70	142.2868	36.6937	2544	2016/09/22 – 2017/10/15	HAK
FKOB1	142.5800	36.8055	4550	2016/09/28 – 2017/10/15	UME
FKOB2	142.8553	36.7225	5506	2016/09/28 – 2017/10/14	HAK
G15	143.5215	37.6773	5239	2016/10/02 – 2017/10/19	UME

^aUME: Paroscientific Series 8CB intelligent type pressure sensor + Umezawa-Musen Co. data logger, HAK: Paroscientific Series 8B pressure sensor + Hakusan Co. LS9150 data logger

^b Station G17 and AoA60 are installed at almost identical location.